J. Fluid Mech. (2009), *vol.* 637, *pp.* 73–104. © Cambridge University Press 2009
doi:10.1017/S0022112009008155

Experimental study of flow separation in laminar falling liquid films

GEORG F. DIETZE†, F. AL-SIBAI AND R. KNEER

Institute of Heat and Mass Transfer, RWTH Aachen University, Aachen 52056, Germany

(Received 15 November 2008; revised 9 May 2009; accepted 10 May 2009; first published online 18 September 2009)

In a previous publication, Dietze, Leefken & Kneer (*J. Fluid Mech.*, vol. 595, 2008, p. 435) showed that flow separation takes place in the capillary wave region of falling liquid films. That investigation focused on the mechanistic explanation of the phenomenon mainly on the basis of numerical data. The present publication for the first time provides clear experimental evidence of the phenomenon obtained by way of highly resolving velocity measurements in a specifically designed optical test set-up. Characteristically, the refractive index of the working fluid was matched to that of the glass test section to provide optimal access to the cross-section of the film for the employed optical velocimetry techniques, namely, laser doppler velocimetry (LDV) and particle image velocimetry (PIV). Using LDV, time traces of the streamwise velocity component were recorded in high spatial (0.025 mm) and temporal resolutions (0.4 ms) showing negative velocity values in the capillary wave region. In addition, simultaneous film thickness measurements were performed using a Confocal Chromatic Imaging (CCI) technique enabling the correlation of velocity data and wave dynamics. Further, using PIV the spatio-temporal evolution of the velocity field in the cross-section of the film was measured with high spatial (0.02 mm) and temporal (0.5 ms) resolutions yielding insight into the topology of the flow. Most importantly these results clearly show the existence of a separation eddy in the capillary wave region. Due to the high temporal resolution of the PIV measurements, enabled by the use of a high-speed camera with a repetition rate of up to 4500 Hz, the effect of wave dynamics on the velocity field in all regions of the wavy film was elucidated. All experiments were performed using a dimethylsulfoxide (DMSO)–water solution and focused on laminar vertically falling liquid films with externally excited monochromatic surface waves. Systematic variations of both the Reynolds number ($Re = 8.6$–15.0) and the excitation frequency ($f = 16$–24 Hz) were performed. Results show that an increase in the wavelength of large wave humps, produced either by an increase in the Reynolds number or a decrease in the excitation frequency, leads to an increase in the size of the capillary separation eddy (CSE). Thereby, the CSE is shown to grow larger than the local film thickness, assuming an open shape with streamlines ending at the free surface.

1. Introduction

Falling liquid films have been investigated extensively in multiphase fluid dynamics ever since the pioneering works of Nusselt (1916) and Kapitza (1948). For a review

† Present address: Institute of Heat and Mass Transfer, 18 Eilfschornsteinstrasse, Aachen, Germany. Email address for correspondence: dietze@wsa.rwth-aachen.de

https://doi.org/10.1017/S0022112009008155 Published online by Cambridge University Press

of contributions see Alekseenko, Nakoryakov & Pokusaev (1994) and Chang & Demekhin (2002). In recent years, numerical and experimental investigations have focused on temporally resolving the influence of surface waves on transport processes in the liquid film. On the numerical side, highly resolved simulations of the full Navier–Stokes equations were performed by Miyara (1999), Gao, Morley & Dhir (2003) and Kunugi & Kino (2005). For example, Kunugi & Kino (2005) present the first full scale three-dimensional simulation of a falling liquid film showing the effect of surface waves on wall shear stress. Experimentally, Mudawar & Houpt (1993*b*) and Adomeit & Renz (2000) performed velocity measurements in the film whereas comprehensive film thickness measurements have been published for example by Liu, Paul & Gollub (1993) and Lel, Al-Sibai & Leefken (2005).

More recently the phenomenon of backflow in the capillary wave region of liquid films and its effect on scalar transport has been elucidated. The existence of this phenomenon was first postulated in principle by Kapitza (1948) and later by Portalski (1964). The first detailed investigation of the backflow phenomenon was performed by Adomeit, Leefken & Renz (2000). The authors experimentally visualized loop-shaped particle path lines in the capillary wave region. Further, they show a significant increase of the local heat transfer coefficient based on numerical data. Since then, Kunugi & Kino (2005) and Kunugi, Kino & Serizawa (2005) performed numerical investigations, establishing a link between the backflow phenomenon evidenced by a sign change in the wall shear stress and the intensification of heat transfer. Tihon *et al.* (2006) directly measured the wall shear stress with an electrodiffusion sensor also detecting a sign change in the capillary wave region. Most recently, Dietze, Leefken & Kneer (2008) provided a mechanistic explanation of the backflow phenomenon and its origin. Based on experimentally validated numerical data the authors show that backflow is the result of flow separation caused by an adverse pressure gradient itself induced by the strong third-order deformation (i.e. change in curvature) of the liquid–gas free surface in the capillary wave region. They also show the initiation and growth of the resulting capillary separation eddy (CSE) during wave development. Further, the paper presents laser doppler velocimetry (LDV) measurements in the falling film that indicate the existence of the CSE. Since then, the CSE in its developed state has also been observed by Malamataris & Balakotaiah (2008) based on numerical simulations.

The present paper constitutes a logical continuation of the investigations presented in Dietze *et al.* (2008). The focus here is the detailed experimental investigation of the CSE phenomenon complementing mainly the numerical results of the stated publication. In order to meet the extremely high requirements with respect to temporal and spatial resolutions dictated by the investigated phenomenon (the crosswise size of the CSE is of the order of 200 μm), an optical test section was specifically designed. The test section enables the implementation of optical measurement techniques such as PIV (particle image velocimetry) and LDV for velocity measurements and a Confocal Chromatic Imaging (CCI) technique for film thickness measurements. These techniques are established for measurements in liquid films. Mudawar & Houpt (1993*b*), Elsässer (1998) and Leefken, Al-Sibai & Renz (2004), for instance, have previously employed LDV for measurements in films. PIV measurements in films were performed by Adomeit & Renz (2000) and Alekseenko *et al.* (2007) whereas film thickness measurements with the CCI technique have been reported by Lel *et al.* (2005) and Dietze *et al.* (2008). However, the implementation of these techniques in the specifically designed optical test section enables an unprecedented spatial resolution of the falling liquid film.

https://doi.org/10.1017/S0022112009008155 Published online by Cambridge University Press

The investigation of the CSE phenomenon is of importance to the development of simplified models of falling liquid films due to its effect on scalar transport on the one hand and its possibly significant effect on the wave dynamics. Advances in film flow modelling have recently been published by Mudunuri & Balakotaiah (2006), Scheid, Ruyer-Quil & Manneville (2006) considering three-dimensional wave dynamics and by Trevelyan *et al.* (2007) considering heat transfer. These models rely on the parameterization of the velocity profile in the film. The detailed experimental investigations of the velocity field and the CSE presented in this work could help to identify adequate approaches to this approximation task. Using the optical test section, film thickness and velocity measurements in two-dimensional vertically falling liquid films with externally excited surface waves were performed for different flow conditions. Thereby, the Reynolds number was varied between 8.6 and 15.0 and the excitation frequency between 16 and 24 Hz.

The paper is structured as follows. In § 2, the optical test section central to this work is introduced with special attention to the matching of refractive indices. Further, all employed measurement techniques are described. Experimental results are presented in § 3. Thereby, § 3.1 introduces film thickness measurement data for the considered flow regimes creating an overview of the wave dynamics encountered in this work. In § 3.2, PIV results clearly proving the existence of the CSE phenomenon and elucidating its dynamics are presented. In § 3.3, the correlation of film thickness and streamwise velocity in the liquid film's residual layer is investigated based on the LDV data. Complementing the PIV results from § 3.2, § 4 presents numerical results showing the spatio-temporal evolution of the CSE during wave development. Conclusions are drawn in § 5.

2. Experimental

2.1. *Optical test set-up*

In order to access the film cross-section with optical velocity and film thickness measurement techniques a specifically designed optical test section (see figure 1) was employed. The principal element of the test section consists of a cuboid quartz glass body that contains a cylindrical bore (the glass body was machined by Aachener Quarz-Glas Technologie Heinrich using the material HSQ300 produced by Heraeus Quarzglas GmbH & Co. KG) creating an inner surface along which the liquid film develops (see figure 2). This configuration provides optical access to the film from all four faces of the glass body. To enable the distortion-free imaging of the film cross-section the refractive indices of working fluid and quartz glass were matched. This was achieved by the careful choice of an appropriate working fluid. Refractive index matching (RIM) is commonly employed for optical measurements in fluid dynamics and a comprehensive review of optically matched systems consisting of a glass material and a working liquid can be found in Budwig (1994) and Albrecht *et al.* (2003). In general, two RIM approaches are possible. When the working liquid is a pure substance the adaptation of refractive indices can be achieved by regulating the temperature. This is possible because the refractive index of most glass materials increases with temperature as opposed to most liquids which exhibit a refractive index decreasing with temperature. On the other hand, the use of mixtures consisting of two or more liquids enables RIM through the regulation of the mixture composition. In the context of the work presented here these two approaches were combined. The employed working fluid consists of an aqueous solution of dimethylsulfoxide (DMSO) whereby the composition of the solution is chosen such that RIM approximately

https://doi.org/10.1017/S0022112009008155 Published online by Cambridge University Press

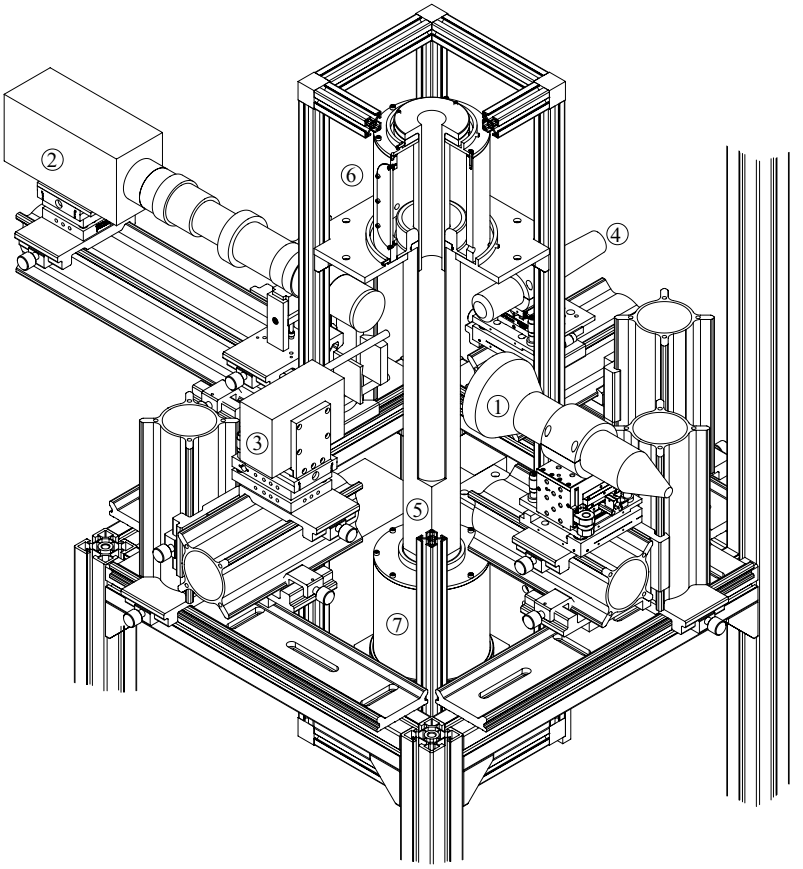


FIGURE 1. Isometric view of the optical test setup including optical measurement instruments. 1: optical emitter–receiver for LDV; 2: high-speed camera with microscopic lens assembly for PIV; 3: light sheet optics for PIV; 4: optical emitter–receiver for film thickness measurements; 5: glass body with rectangular outer perimeter and circular inner perimeter; 6: middle reservoir including film inlet; 7: lower reservoir.

takes place at room temperature. The precise adaptation of the refractive index is then achieved through the regulation of the working temperature. Adomeit & Renz (2000) previously employed pure DMSO for measurements in falling liquid films in a similar optically matched set-up. However, they employed a cylindrical glass tube as opposed to the glass body shown in figures 1 and 2 creating the need for further optical measures to enable distortion-free imaging.

In addition to the DMSO–water solution which was used to investigate the CSE phenomenon, an aqueous glycerol solution was employed. Using this working fluid (due to its large kinematic viscosity) conditions of smooth developed film flow could be achieved in the optical test section at $Re \approx 1$. By measuring the crosswise velocity profile under these conditions the LDV measurement technique was validated on the basis of the analytical solution for smooth developed film flow. Table 1 displays the properties of the two working fluids (i.e. density ρ, surface tension σ and kinematic viscosity ν) as well as the respective solution compositions and the RIM temperature which was determined with an *in situ* refraction experiment using the laser beam employed for the LDV measurements. In addition, the refractive index of the quartz glass as well as that of the two working fluids was measured as a function of

https://doi.org/10.1017/S0022112009008155 Published online by Cambridge University Press

Solute	Mass fraction (%)	T (°C)	$\rho\,(\mathrm{kg\,m^{-3}})$	$\sigma\,(\mathrm{N\,m^{-1}})$	$\nu\,(\mathrm{m^2\,s^{-1}})$	$Ka = \sigma\rho^{-1}g^{-1/3}\nu^{-4/3}$
DMSO	83.11	25.2	1098.3	0.0484	2.85×10^{-6}	509
Glycerol	90.98	32.6	1230.7	0.0635	93.77×10^{-6}	6

TABLE 1. Fluid properties of the two refractively matched aqueous solutions employed as working fluids (all measurements were performed at RIM temperature with liquid samples containing the tracer particles used for velocity measurements).

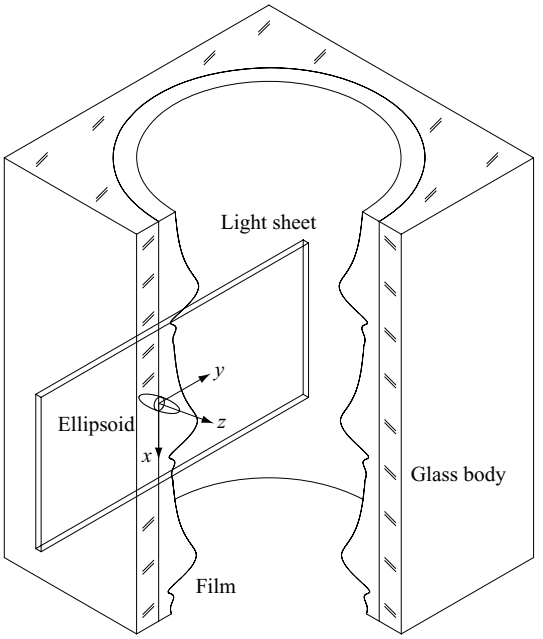


FIGURE 2. Enlarged view of the falling liquid film flowing down the inside of the glass body showing the thin light sheet used for PIV and the LDV-ellipsoid (objects are individually scaled to illustrate geometrical conditions and size relations between different objects are incorrect).

temperature with an Abbe refractometer at wavelengths $\lambda = 514.5$ and 488.0 nm (laser wavelengths employed for LDV and PIV in this work are $\lambda = 514.5$ and 511.6 nm, respectively). The corresponding experimental data are plotted in figure 3 whereby the points of intersection of the different curves define the RIM temperature.

The optical test section displayed in figure 1 is integrated into a standard closed circuit test set-up. Thereby, the working fluid is pumped from the lower reservoir (item 7 in figure 1) to an upper buffer reservoir situated above the optical test section by a gear pump. This reservoir is equipped with an overflow allowing for the damping of flow rate oscillations and decouples the pressurized part of the circuit from the falling film section as the liquid leaving the reservoir is accelerated only by gravity. In order to regulate the working fluid temperature, a heat exchanger is integrated into the circuit between the lower and upper reservoirs. The liquid in the secondary circuit of the heat exchanger is thermally regulated with a laboratory thermostat, limiting temperature variations to ± 0.01 K. The volume flow rate is measured with a positive displacement flow metre between the heat exchanger and the upper reservoir. For all experiments the ambient temperature of the laboratory was conditioned to $T = 25$°C.

https://doi.org/10.1017/S0022112009008155 Published online by Cambridge University Press

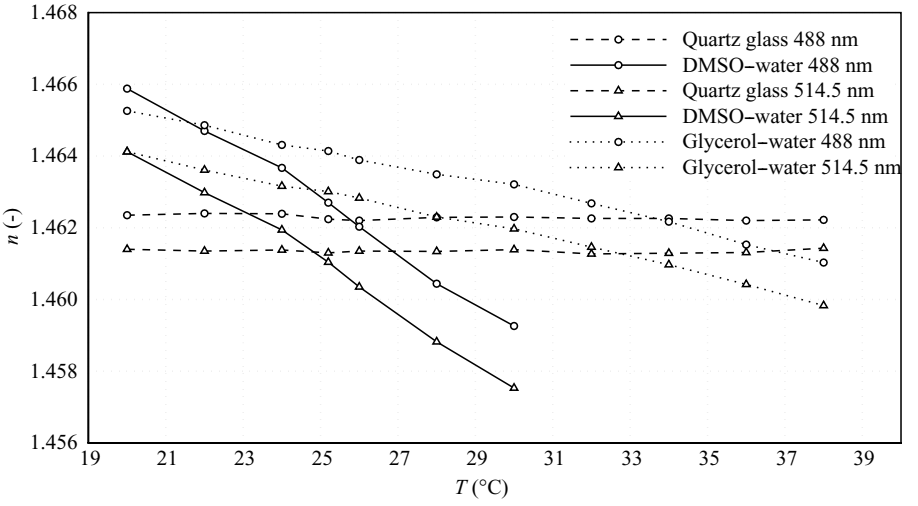


FIGURE 3. Temperature dependence of the refractive index for glass body and DMSO–water solution at wavelengths $\lambda = 488$ and 514.5 nm.

The flow of working fluid leaving the upper reservoir is divided and radially fed to the middle reservoir shown in figure 1 through two separate entry ports. Upon entering the middle reservoir the liquid impinges on a cylindrical overflow further dissipatively damping flow oscillations. The inner surface of the overflow is rounded in order to avoid flow separation as the working fluid enters the glass body. The actual inlet for the falling liquid film consists of an annulus created between the glass body and a cylindrical inset. The thickness of the annular inlet channel can be varied incrementally through the choice of the inset diameter. Further, the radial position of the inset as well as the orientation of its axis can be precisely set with micrometric set screws (not pictured in figure 1). Using these set screws, the cylindrical inset was oriented concentrically to the glass body bore before each measurement series in dry state. For this, the film thickness measurement technique described in the following subsection was employed to evaluate the annulus thickness variation in the axial direction. In a second step, the radial inset orientation was optimized by visually evaluating the azimuthal uniformity of wavefronts once the film flow had developed. Finally, before each measurement series, it was verified that the amplitude of measured film thickness time traces for the respective lowest frequency waves did not deviate by more than 3 % from values predicted by the empirical correlation of Nosoko *et al.* (1996). The air volume above the liquid level developing in the middle reservoir is connected to an external loudspeaker-driven resonator enabling the monochromatic excitation of surface waves in the film flow. Finally, the temperature of the liquid in the middle reservoir is measured with a resistive thermometer (Pt 100) with an error of ± 0.1 K.

2.2. *Measurement techniques*

Three measurement techniques were employed in the present work, namely, LDV and PIV for velocity measurements and a film thickness measuring technique based on Confocal Chromatic Imaging (CCI). The principles of these measurement techniques are well established in the literature (see, e.g. Albrecht *et al.* 2003; Raffel *et al.* 2007; Cohen-Sabban, Gaillard-Groleas & Crepin 2001) and attention here shall be

https://doi.org/10.1017/S0022112009008155 Published online by Cambridge University Press

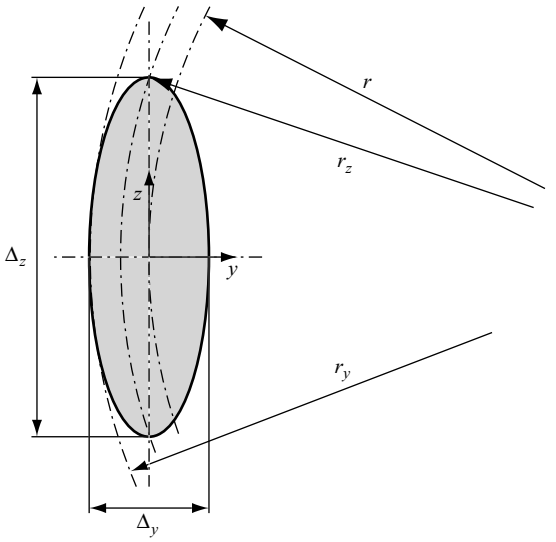


FIGURE 4. Sketch of the LDV measurement ellipsoid with Cartesian and radial coordinates. The origin of the radial coordinate is situated on the axis of the glass body bore and the dimensions of the ellipsoid are $\Delta_x = \Delta_y = 25$ μm and $\Delta_z = 150$ μm, respectively.

focused merely on their specific application to the optical test section employed in this work.

LDV was employed for point measurements of streamwise velocity time traces. A standard LDV system (comprising emitting and receiving optics as well as processing hardware and software purchased from Dantec Dynamics A/S, and a Spectra-Physics Argon-Ion Laser) was used in back scattering mode at a laser wavelength of $\lambda = 514.5$ nm. Due to this configuration a data rate of approximately 3000 Hz was achieved, adequately resolving the surface waves excited with frequencies of the order of 10 Hz. In principle, the same optical set-up as described in Dietze *et al.* (2008) was employed. However, a significant (sixfold) increase in the crosswise spatial resolution of the measurement was achieved by orienting the ellipsoidal measurement volume such that its longest axis points in z-direction as shown in figure 2. This is only possible as the optical test section provides access to the film flow from four sides. The size of the ellipsoid in y- and x-directions thereby is $\Delta_x = \Delta_y = 25$ μm as opposed to a size of $\Delta_z = 150$ μm in z-direction. It should be noted here that the minimal film thickness in the context of this work (which is associated with the capillary wave region and thus with the CSE) is approximately 200 μm (see § 3.1). The extent of the measurement volume in z-direction does not limit the spatial resolution of the measurement as changes of the velocity in z-direction are negligible in the considered case of two-dimensional waves. Variation over the z-axis of the ellipsoid takes place solely due to the fact, that the film flow is cylindrical and not Cartesian (see figure 4). It shall be shown here on the basis of a smooth developed cylindrical film flow that this effect is negligible. For this case the radial distribution of the streamwise velocity component is given by (see Mudawar & Houpt 1993*a*)

$$u(r) = \frac{1}{2}\frac{g}{\nu}\left[\frac{1}{2}(R^2 - r^2) - R_\delta^2 \ln\left(\frac{R}{r}\right)\right], \tag{2.1}$$

https://doi.org/10.1017/S0022112009008155 Published online by Cambridge University Press

where $R = 24.46$ mm is the radius of the glass body bore and R_δ the radius of the free surface of the film which depends on the flow regime, while r designates the radial coordinate. Following (2.1), the ratio between velocity variations over the measurement volume in y- and z-directions is

$$\frac{\Delta u_z}{\Delta u_y} = \frac{u|_r - u|_{r=r_z}}{u|_r - u|_{r=r_y}} = \frac{0.5\,\left(r_z^2 - r^2\right) - R_\delta^2\,\ln\left(r_z/r\right)}{0.5\,\left(r_y^2 - r^2\right) - R_\delta^2\,\ln(r_y/r)} \qquad (2.2)$$

$$r_z = \left(r^2 + 0.25\,\Delta_z^2\right)^{0.5}, \quad r_y = r + 0.50\,\Delta_y$$

where geometric quantities are illustrated in figure 4. Assuming a film thickness of $\delta = R - R_\delta = 300$ μm (corresponding to the mean film thickness of the falling liquid films considered in this work; see § 3.1) evaluation of the above relation at $r = R$ (where the gradient of the velocity profile is maximal) yields $\Delta u_z/\Delta u_y = 0.009$. The velocity variation in z-direction is thus roughly two orders of magnitude smaller than the corresponding variation in y-direction.

Solid tracer particles of titanium dioxide with a mean diameter of $d_P = 2$ μm and a density of 4500 kg m^{-3} were employed. As established in Dietze *et al.* (2008) fluid elements in the CSE region follow loop-shaped path lines of small characteristic length. In order to ensure that the LDV measurements resolve the CSE phenomenon accurately it is necessary to assess the ability of the tracer particles to follow the flow in the region of interest. This was done on the basis of the Basset–Boussinesq–Oseen (BBO) equation which governs the movement of a particle in a non-steady flow. Hjelmfelt & Mockros (1966) derived the frequency response of the particle velocity to an oscillation in fluid velocity from the BBO equation. This result enables the computation of the amplitude ratio η and the angular phase shift $\Delta\phi$ between the particle and fluid velocity oscillations for a given excitation frequency. Both quantities are indicators for the capacity of the particle to follow the surrounding flow and are plotted in figure 5 as a function of the solid to fluid density ratio s and the Stokes number $St = \Delta t\ \nu/(2\pi\, d_P^2)$. In addition, circles displayed in figures 5(a) and 5(b) highlight points corresponding to the measurement conditions encountered in this work, i.e. titanium dioxide particles dispersed in the DMSO–water solution (see table 1). Thereby, the Stokes number was formulated with the characteristic time of the CSE phenomenon ($\Delta t = 0.001$ s). From the figures, the conclusion can be drawn that under the conditions considered here the employed tracer particles follow the liquid flow well.

Finally, the LDV measurement set-up was validated on the basis of measurements performed in a smooth developed film flow using the water–glycerol solution detailed in table 1. The crosswise profile of the streamwise velocity under these conditions is given by the analytical solution in (2.1) (R_δ was thereby obtained by integrating (2.1) and iteratively solving it for the volume flow rate). Figure 6 illustrates a comparison for $Re \approx 1$ between this analytical solution and measurement data obtained by LDV, showing good agreement between the two data sets. Further, it can be observed that the standard deviation of the measurement data for a given measurement position is negligible in relation to the measured velocity which is due to the extremely high spatial resolution of the set-up. The different measurement positions were adjusted using a three-axis micrometric traversing system as shown in figure 1 in incremental steps of 20 μm with a positioning error of only ± 0.1 μm in all directions.

PIV was used to measure the velocity field in the x–y plane as a function of time. In addition to the LDV data this technique provides an understanding of the

https://doi.org/10.1017/S0022112009008155 Published online by Cambridge University Press

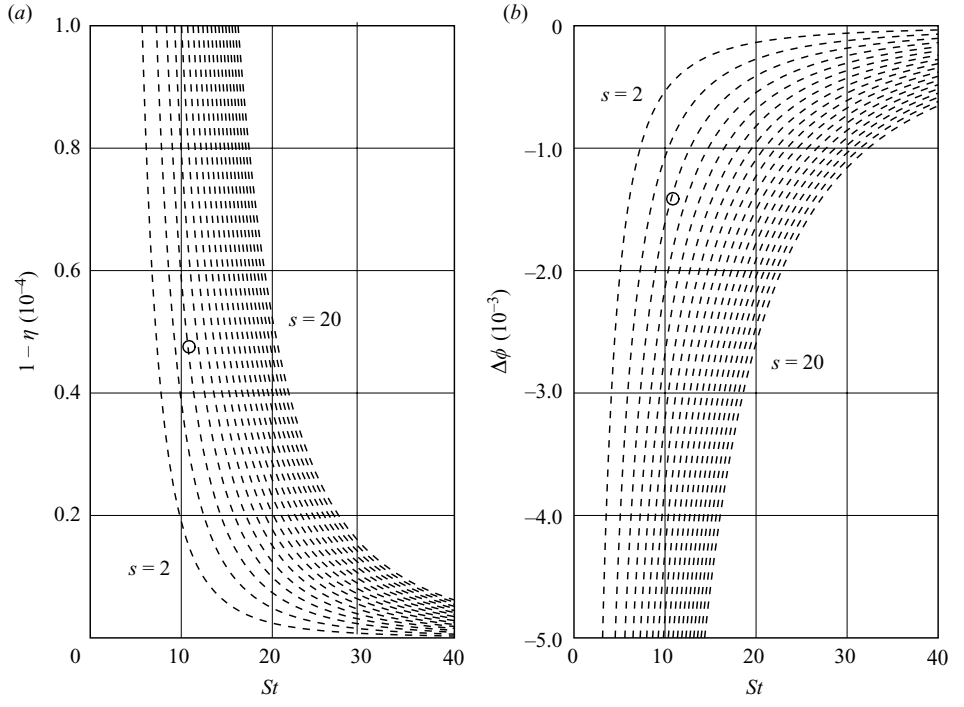


FIGURE 5. (*a*) Amplitude ratio η and (*b*) angular phase shift $\Delta\phi$ for the frequency response of a spherical particle subjected to an oscillating flow as a function of the solid to fluid density ratio s and the Stokes number St. Curves represent solutions of the Basset–Boussinesq–Oseen equation obtained according to Hjelmfelt & Mockros (1966). Circles highlight points corresponding to the considered case of titanium dioxide particles suspended in the DMSO–water solution (St formulated with the characteristic time of the CSE phenomenon, i.e. 10^{-3} s).

topology of the velocity field in the liquid film and more specifically the capillary wave region, yielding clear evidence of the existence of the CSE there. Velocity data were determined with a standard cross-correlation algorithm from pairs of consecutively recorded digital camera images of the particle-laden (the same tracer particles as for LDV measurements were employed) film flow illuminated with a thin laser light sheet (thickness: 1 mm). The cross-correlation algorithm was applied to raw images using consecutively refined interrogation areas with a final size of 6 × 6 picture elements. For the final cross-correlation step no interrogation area overlap was exploited. Computed vectors were validated by median filtering (see Westerweel 1994), whereby vectors with lengths differing from the median of neighbouring interrogation area values by more than twice the root mean square of the latter were discarded. Further, the detectability of cross-correlation peaks (i.e. the ratio of the two largest peaks of the cross-correlation function) exceeds the value 1.2. Because standard calibration by means of a calibration target was not feasible due to the geometric constraints of the optical test section, PIV measurements were calibrated with corresponding LDV data once for every measurement series. For this, velocity data at characteristic points, which are detectable both in LDV time traces and PIV vector plots (more specifically these points are extremal velocity values in the capillary wave region) were employed. Light sheet optics and orientation of the light sheet are illustrated in figures 1 and 2, respectively. Direct reflection of laser light by the free surface did not pose a problem as the latter is only slightly curved in azimuthal direction and thus reflects

https://doi.org/10.1017/S0022112009008155 Published online by Cambridge University Press

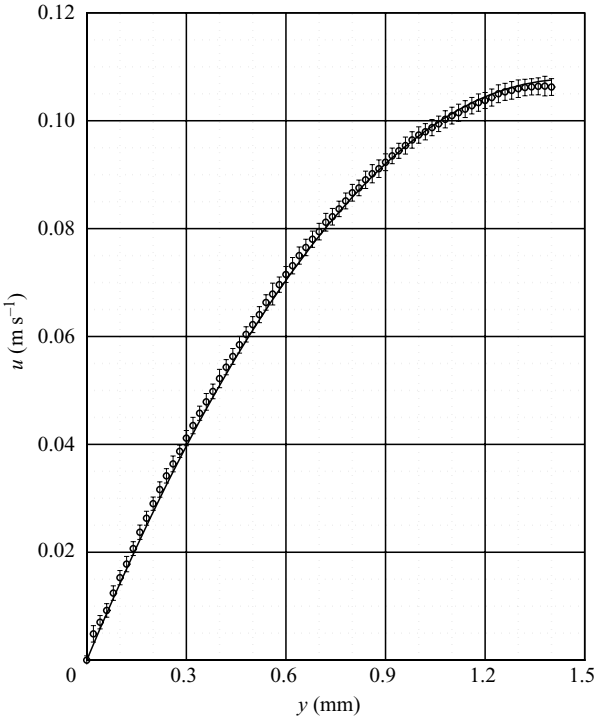


FIGURE 6. Radial profile of the streamwise velocity component u for a smooth water-glycerin film (see table 1) for $Re = 1.07$. ○, experimental data (bars illustrate standard deviation of measurement data); —, analytical solution for smooth developed cylindrical film flow (see e.g. Mudawar & Houpt (1993*a*)).

incident light away from the lens assembly. However, reflections at the interface of light scattered by particles adhering to the wall were visible in camera images after sustained operation of the set-up when a particle layer had formed at the wall. Because the free surface is concave in azimuthal direction such reflections did not limit the capacity to resolve the liquid phase velocity field in the x–y plane. Nonetheless, the inner surface of the glass body was cleaned regularly between measurement series to minimize this effect. As light source, a pulsed copper vapour laser (Oxford Lasers Ltd., model CU15-A) with a wavelength of $\lambda = 511.6$ nm was employed whereby the pulse frequency was set to 9000 Hz for all experiments (yielding a pulse length of 10 ns and a pulse energy of 2 mJ). The illuminated section of the film was imaged in z-direction with a high-speed Complementary Metal Oxide Semiconductor (CMOS) camera (Vision Research, Inc., model Phantom v4.3) equipped with a microscopic lens assembly (see figure 1). The lens assembly (Infinity Photo-Optical Company, model K2) allows for a 10-fold magnification of the liquid film resolving the minimal film thickness of $\delta \approx 200$ μm with roughly 100 camera picture elements. The frame repetition rate of the camera was adapted to the flow conditions and varied between 1500 and 4500 Hz whereby only frequencies which the laser frequency is a multiple of were considered. The time of exposure of the camera chip was set to 111 μs which results from the reciprocal value of the laser frequency. These settings ensure that all camera images are illuminated by single laser pulses and that the time difference between successive images is constant. Since two images are needed for the evaluation of the velocity field at a given time the film flow is resolved with half the camera

https://doi.org/10.1017/S0022112009008155 Published online by Cambridge University Press

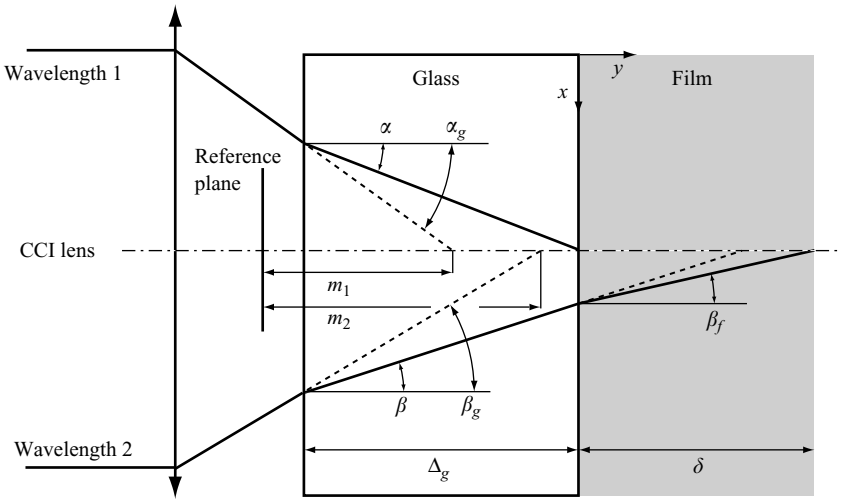


FIGURE 7. Illustration of the optical film thickness measurement showing paths of light beams reflected by the glass wall (wavelength 1) and the free surface of the film (wavelength 2), respectively. Solid lines represent actual beam paths and dashed lines show beam paths in the absence of refraction. The quantities measured by the CCI technique are m_1 and m_2.

frame repetition rate, i.e. between 750 and 2250 Hz compared to a maximal wave frequency of 24 Hz. For all experiments, image sequences of the film spanning several period lengths were recorded enabling the temporal resolution of the effect of wave dynamics on the velocity field within a single wave.

The CCI technique was introduced by Cohen-Sabban *et al.* (2001) as a non-intrusive distance-measuring technique. The set-up consists of an optical probe acting both as receiver and emitter. The probe focuses light from a white light source on to an interval of points due to the chromatic aberration of its front lens. Light reflected back into the receiver by a surface or interface positioned in this interval is thus chromatically selective. The distance information relative to a given reference plane is then obtained by analysing the spectral distribution of the reflected light with a spectrometer. The technique was modified for film thickness measurements in falling liquid films by Lel *et al.* (2005) and Dietze *et al.* (2008). For this work it was further modified to measure the local film thickness as a function of time in the optical test section by accessing the flow through the glass body wall as pictured in figure 7. Using the designations illustrated in the figure the film thickness δ is given by

$$\delta = \left[m_2 - m_1 + \Delta_g \left(\frac{1}{n_g^1} \frac{\cos\alpha_g}{\cos\alpha} - \frac{1}{n_g^2} \frac{\cos\beta_g}{\cos\alpha} \right) \right] n_f^2 \frac{\cos\beta_f}{\cos\beta}. \tag{2.3}$$

For the considered conditions all angles are negligibly small so that the film thickness is given in good approximation by

$$\delta \approx \left[m_2 - m_1 + \Delta_g \left(\frac{1}{n_g^1} - \frac{1}{n_g^2} \right) \right] n_f^2, \tag{2.4}$$

where the numerical indices refer to the two respective wavelengths and m_1 and m_2 designate the quantities actually measured by the CCI device (STIL SA, model CHR 540). Glass thickness Δ_g and distance to the inner wall m_2 were measured before each experiment in dry state whereas the spectral distribution of the refractive indices of quartz glass and working liquid were measured at RIM temperature using an Abbe

https://doi.org/10.1017/S0022112009008155 Published online by Cambridge University Press

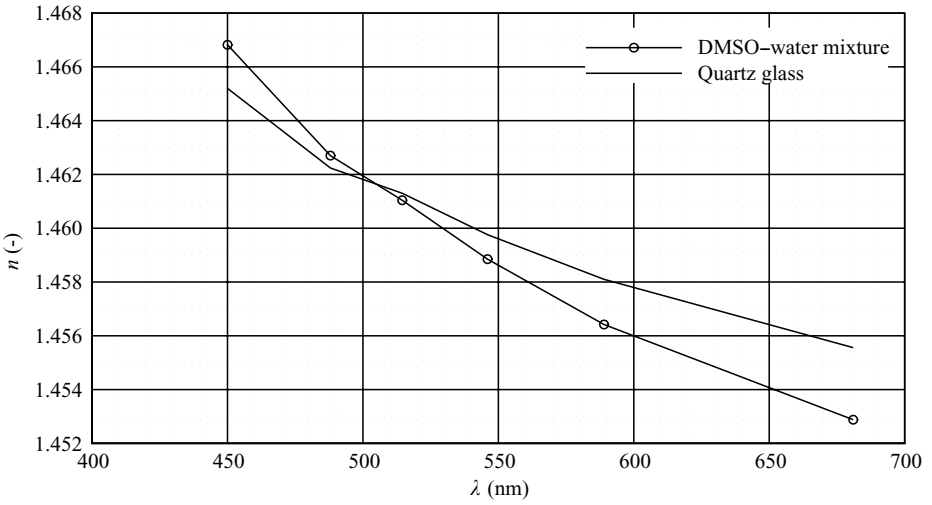


FIGURE 8. Spectral dependence of the refractive index in the visible range for glass body and DMSO–water solution at $T = 25.2\,^{\circ}\mathrm{C}$.

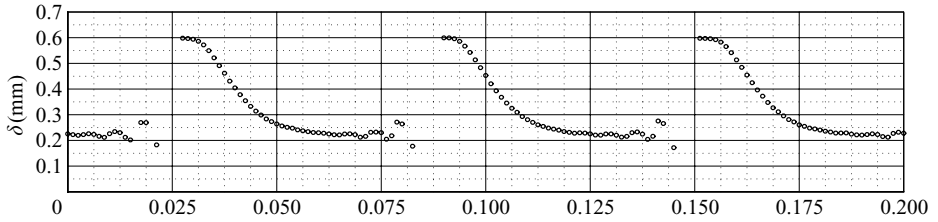
refractometer (see figure 8). Evaluation of the total differential of δ according to (2.4) (with measurement errors of 1 μm for m_1 and m_2 and 0.0002 for the refractive indices) yields an absolute film thickness measurement error of 4 μm. In this configuration, film thickness measurements were performed with an acquisition frequency of 800 Hz. During LDV experiments the film thickness was measured simultaneously (and at the same circumferential position as the LDV) to enable correlation of film thickness and velocity data. Thereby, a small streamwise offset was inevitable to avoid disturbance of the film thickness measurements by the LDV laser beams.

3. Experimental results

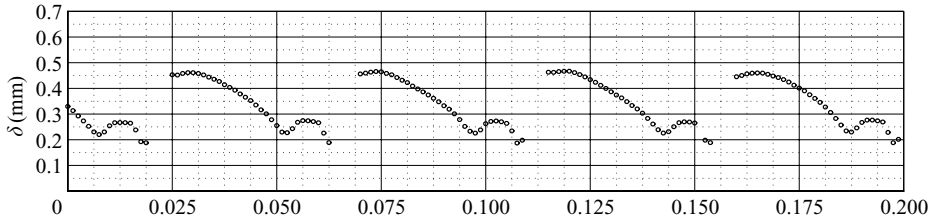
3.1. *Wave dynamics*

Figures 9 and 10 show film thickness time traces of two-dimensional externally excited surface waves measured in the optical test section for different values of the Reynolds number and excitation frequency using the CCI technique (introduced in § 2.2). All measurements in this work were performed at a streamwise position of $x = 120$ mm (measured from the bottom of the cylindrical inset) whereby preliminary experiments showed that for all investigated flow conditions surface waves are developed at that position. The depicted results representatively cover the range of investigated flow conditions. The figures show that both the Reynolds number and the excitation frequency significantly influence the free-surface topology. At $Re = 15.0$ and $f = 16$ Hz (see figure 9(*a*)) for instance the free surface is characterized by large wave humps preceded by three capillary waves. As the frequency is increased to 22 Hz (see figure 9(*b*)) the amplitude of the large waves decreases while all but one of the capillary waves are suppressed. These effects are of course well established in the literature (see Liu *et al.* 1993 and Nosoko *et al.* 1996) and are due to the interaction of large waves as their separation decreases. The same frequency dependence as for $Re = 15.0$ can be observed for lower values of the Reynolds number (see figures 9(*c*)–9(*e*) and 10(*a*)–(*c*)) whereby at high frequencies the wave separation is so small that capillary waves are suppressed altogether (see figures 9(*e*) and 10(*c*)). This of

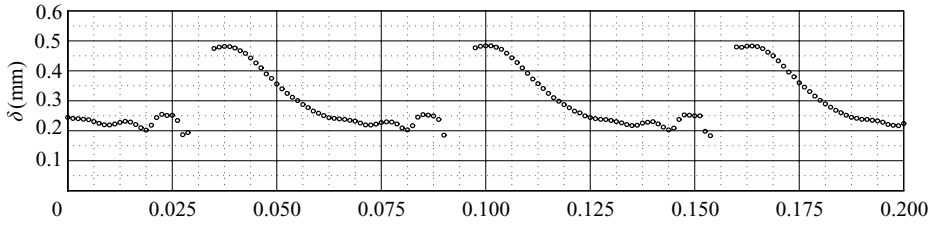
https://doi.org/10.1017/S0022112009008155 Published online by Cambridge University Press



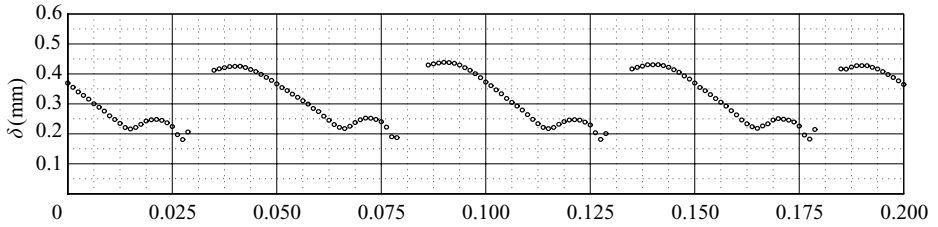
(*a*) $Re = 15.0$, $f = 16$ Hz



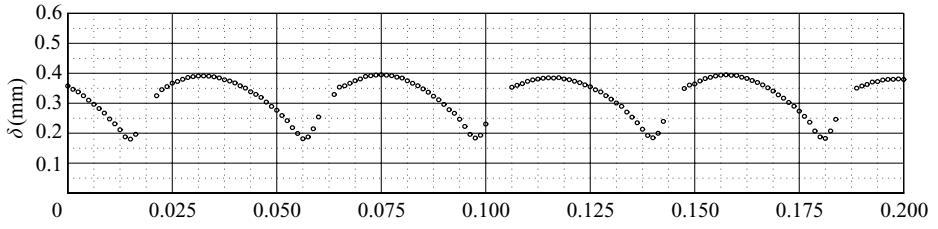
(*b*) $Re = 15.0$, $f = 22$ Hz



(*c*) $Re = 10.7$, $f = 16$ Hz



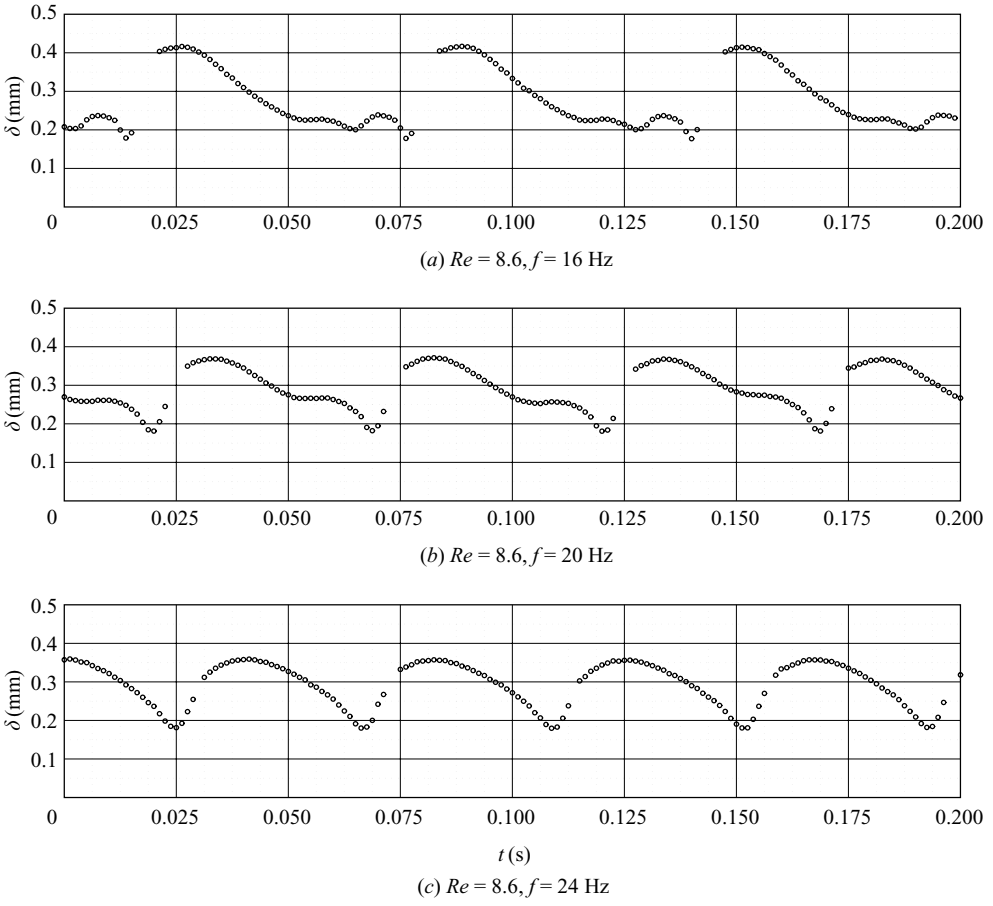
(*d*) $Re = 10.7$, $f = 20$ Hz



(*e*) $Re = 10.7$, $f = 24$ Hz

FIGURE 9. Film thickness time traces measured in the developed region of the liquid film for different values of the Reynolds number and excitation frequency.

https://doi.org/10.1017/S0022112009008155 Published online by Cambridge University Press



(*a*) $Re = 8.6, f = 16$ Hz

(*b*) $Re = 8.6, f = 20$ Hz

(*c*) $Re = 8.6, f = 24$ Hz

FIGURE 10. Film thickness time traces measured in the developed region of the liquid film for different excitation frequencies: $Re = 8.6$.

course significantly affects the CSE phenomenon as will be established in § 3.2. The Reynolds number influence acts contrary to that of the frequency as can be deduced from figures 9(*a*), 9(*c*) and 10(*a*). This is due to the fact that wave separation decreases with frequency yet increases with the Reynolds number (see, e.g. Nosoko *et al.* 1996). Another observation resulting from figures 9 and 10 is that the minimal film thickness (observed in the capillary wave region) is scarcely influenced by the varied quantities.

As can be seen in figures 9 and 10 the film thickness measurements do not resolve wavefronts equally well for all cases (see for instance figures 9(*a*)–9(*d*)). This is due to a combination of effects linked to the large wavefront inclination angle for the cases in question. On the one hand, the intensity of light reflected back into the CCI emitter–receiver decreases with increasing steepness of the wavefront due to elementary geometrical optics. On the other hand, as the wavefronts grow steeper their transit time in x-direction decreases, thus reducing the number of measurement points captured by the measurement device (operating at a constant acquisition frequency). In addition, steeper wavefronts coincide with larger values of the wave celerity also causing the transition time to decrease. It is also discernible from the film thickness time traces that capillary wavefronts of comparable steepness are resolved better

https://doi.org/10.1017/S0022112009008155 Published online by Cambridge University Press

than large wavefronts. This results from the fact that free surface signal intensity is larger for capillary wave fronts as the distance to the CCI emitter–receiver is smaller compared to large wavefronts.

3.2. *CSE dynamics*

After having delimited the wave dynamics encountered in the context of this work, attention here is directed towards the velocity field in the liquid film cross-section which was measured by way of PIV (see § 2.2). Thereby, the elucidation of the velocity field in the capillary wave region is of particular interest. In order to distinguish different subregions of the capillary wave region some appropriate terminology shall be introduced. Consequently, capillary waves shall be numbered in ascending order with increasing streamwise position relative to the main wave to which they belong. Further, the terms capillary maximum and minimum shall pertain to the maximum and minimum values of the film thickness in the corresponding capillary wave.

Figure 11 depicts velocity vectors in the liquid film cross-section for flow conditions corresponding to figure 9(a) (i.e. $Re = 15.0$, $f = 16$ Hz). Different images capture the velocity field at different times in the evolution of a surface wave. Thereby, the vector plots are arranged in the order in which an observer would see the corresponding wave regions pass by, starting with the second capillary minimum (figure 11(a)) and ending with the large wave (figure 11(d)). In each subfigure the free surface of the film determined from PIV images is displayed and a pictogram, highlighting the considered region of the film is incorporated. Also, underneath each pictogram, a reference vector of adequately chosen length is displayed.

Figure 11(a) depicting velocity vectors in the region of the second capillary minimum shows a strong deceleration and subsequent reacceleration of the flow in streamwise direction. This is evidenced by the small velocities at the capillary minimum as well as the fact that upstream of the minimum vectors point away from the wall ($\partial u/\partial x < 0 \leftrightarrow \partial v/\partial y > 0$) whereas they point towards the wall further downstream ($\partial u/\partial x > 0 \leftrightarrow \partial v/\partial y < 0$). As reported in Dietze *et al.* (2008) the cause of this deceleration and reacceleration is the increase and subsequent decrease of the wall pressure governed by the streamwise change in free surface curvature. Thereby, the governing adverse pressure gradient is induced by the change in free surface curvature between wave trough (where it is positive) and the following wave crest (where it is negative). The flow near the first capillary maximum (see figure 11(b)) is accelerated and subsequently decelerates as it nears the second capillary minimum. Flow velocities attain considerably larger values as in figure 11(a) which is due to the stronger change in free surface curvature.

In the region of the first capillary minimum, pictured in figure 11(c) the change in free surface curvature is so large that the resulting adverse pressure gradient leads to flow reversal and the development of a CSE. Thereby, the vector plot in figure 11(c) constitutes the first clear experimental evidence of the existence of flow separation in the capillary wave region of falling liquid films. The size of the CSE is such that it is not entirely contained in the liquid film, assuming an open shape with streamlines ending at the free surface. The possibility of such a scenario was first established by Rood (1994), who investigated vortex interactions with a free surface.

Rood (1994) states that when a vortex breaks up and attaches to a free surface, interfacial vorticity transport takes place. This interfacial vorticity transport also takes place in the CSE region under consideration (and displayed in figure 11(c)) as is evident when evaluating the associated out of plane vorticity component $\omega_z = \partial v/\partial x - \partial u/\partial y$, contours of which are displayed in figure 12(b). In order to calculate ω_z the

https://doi.org/10.1017/S0022112009008155 Published online by Cambridge University Press

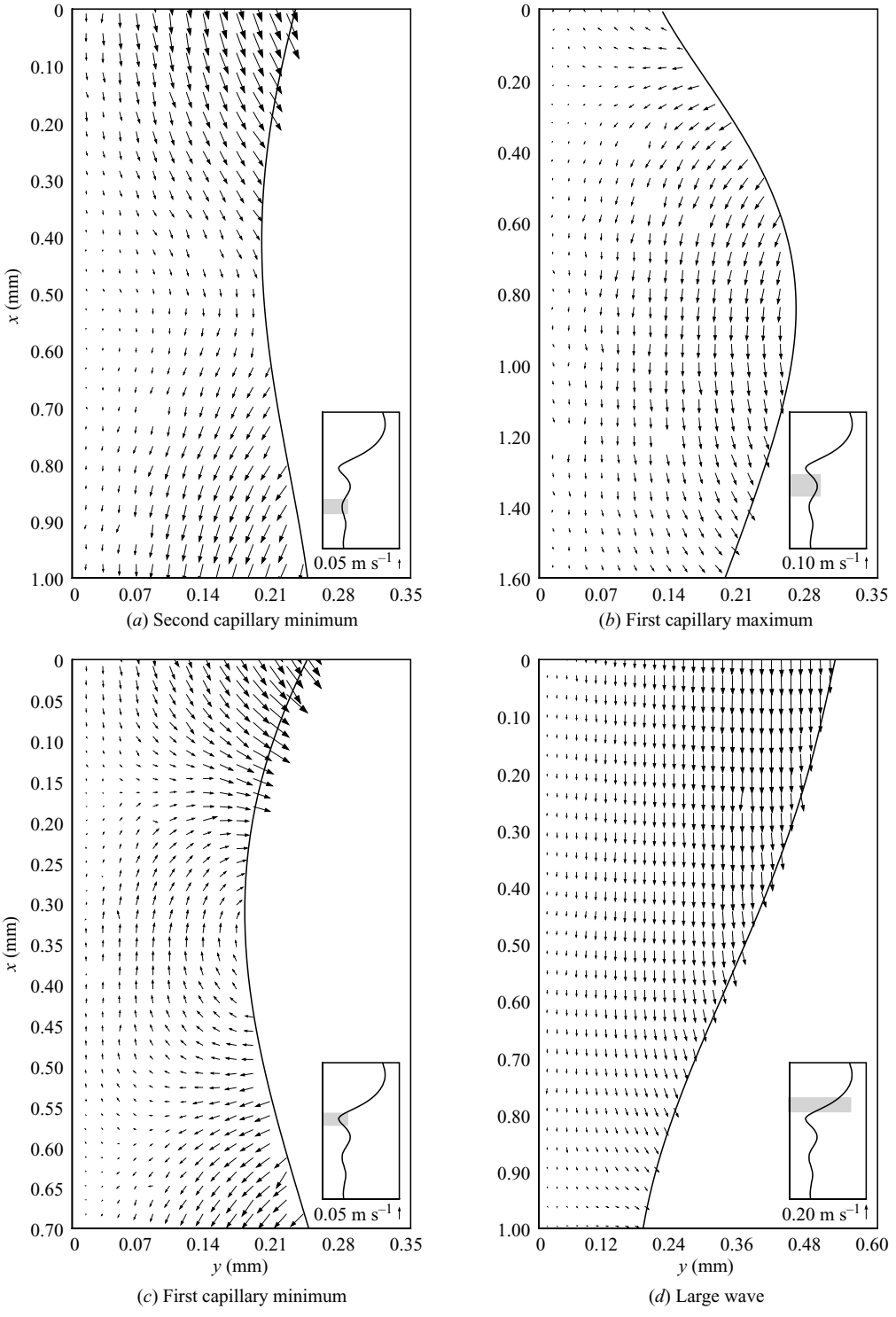


FIGURE 11. Velocity vectors in the cross-section of the liquid film at different times in the evolution of a surface wave measured with PIV: $Re = 15.0$, $f = 16$ Hz (subfigures are scaled differently).

https://doi.org/10.1017/S0022112009008155 Published online by Cambridge University Press

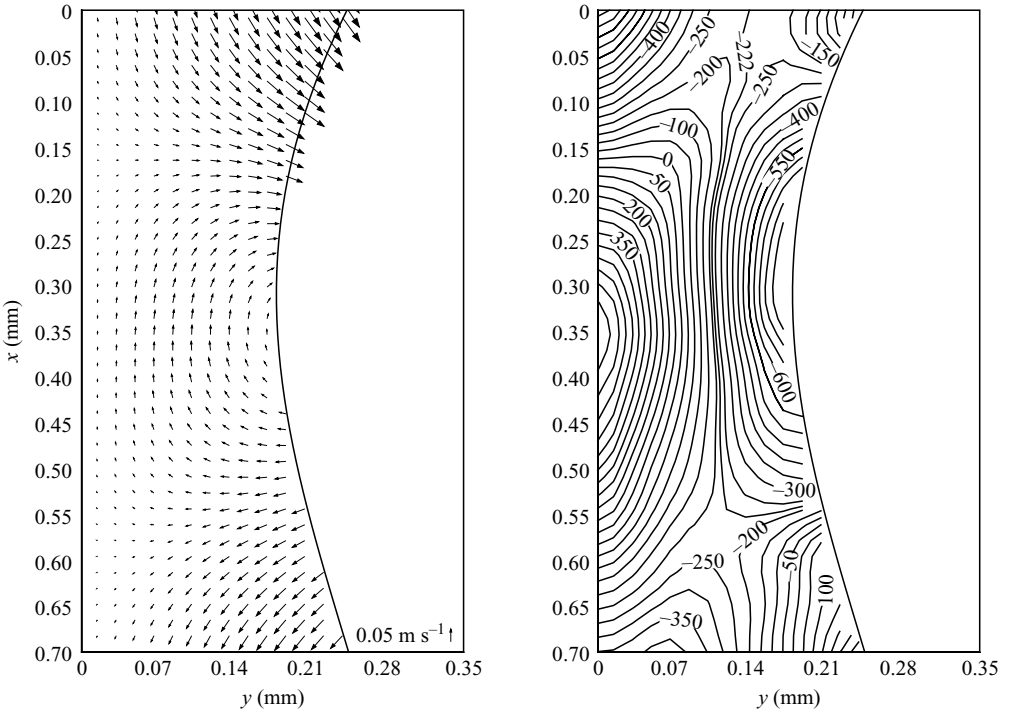


FIGURE 12. Smoothed velocity field resulting from the application of a moving average filter to the raw velocity data of figure 11(*c*) and contour plot of the out of plane vorticity component $\omega_z = \partial v/\partial x - \partial u/\partial y$ derived from the smoothed field.

velocity field of figure 11(*c*) was smoothed with a moving average filter (which takes into account only the immediate crosswise and streamwise neighbours of a considered data point), yielding the velocity plot displayed in figure 12(*a*). The necessity of smoothing PIV velocity data in order to obtain vorticity fields was discussed by Luff *et al.* (1999). The derivatives $\partial v/\partial x$ and $\partial u/\partial y$ were approximated by their first-order central difference discretization (forward or backward difference discretization was employed at the boundaries, depending on available neighbouring data points). Because it is derived from smoothed velocity data, the contour plot in figure 12(*b*) should be considered only as a qualitative indicator of vorticity distribution in the CSE region. It shows that the CSE is divided into two distinct vorticity regions (in what follows the term vorticity shall be used to designate ω_z) which can be clearly attributed to the mechanisms of vorticity generation at the wall (see, e.g. Morton 1984) and the free surface (see Wu 1995), respectively. At the wall, vorticity is generated by the resulting action of adverse streamwise pressure gradient and gravitational acceleration (see also Green 1996), the local vorticity flux (i.e. vorticity per unit time and unit area) normal to the wall is then given by

$$-\nu\frac{\partial\omega_z}{\partial y} = \frac{1}{\rho_l}\frac{\partial p}{\partial x} - g, \tag{3.1}$$

where the terms on the right-hand side constitute the rate of vorticity generation per unit area. In the CSE region, the resulting upstream pressure force on a fluid element surpasses the downstream gravitational force, which means that positive vorticity

https://doi.org/10.1017/S0022112009008155 Published online by Cambridge University Press

is generated at the wall (i.e. the right-hand side of (3.1) is positive). According to Lundgren & Koumoutsakos (1999), vorticity at the free surface, assuming negligible tangential shear stress, is given by the following relation:

$$\omega_z = -2\,\nabla\cdot\boldsymbol{\tau}\,(\boldsymbol{u}\cdot\boldsymbol{n}) - 2\kappa\,\boldsymbol{u}\cdot\boldsymbol{\tau}, \quad \kappa = \frac{\partial^2\delta/\partial x^2}{(1+(\partial\delta/\partial x)^2)^{3/2}},$$

$$\boldsymbol{n} = (\partial\delta/\partial x,\ -1,\ 0)^T(\partial\delta/\partial x^2+1)^{-1/2}, \boldsymbol{\tau} = (-1,\ -\partial\delta/\partial x,\ 0)^T(\partial\delta/\partial x^2+1)^{-1/2}, \tag{3.2}$$

where $\boldsymbol{n}$ and $\boldsymbol{\tau}$ form an orthonormal surface coordinate system in the x–y plane with $\boldsymbol{n}$ pointing into the liquid phase, and κ designates the interface curvature. From (3.2) it is clear that interfacial vorticity in the CSE region should be negative, which concurs with figure 12(b). In order to identify the generating source of this negative vorticity, the normal vorticity flux at the interface is introduced (see Lundgren & Koumoutsakos 1999 for the derivation)

$$-\nu\,\nabla\cdot\boldsymbol{n}\,\omega_z = -\boldsymbol{u}\cdot\boldsymbol{n}[\nabla\cdot\boldsymbol{\tau}\,(\boldsymbol{u}\cdot\boldsymbol{n}) + \kappa\,\boldsymbol{u}\cdot\boldsymbol{\tau}] - \frac{\mathrm{d}}{\mathrm{d}t}(\boldsymbol{u}\cdot\boldsymbol{\tau}) + \frac{1}{\rho}\nabla\cdot\boldsymbol{\tau}\ p - \boldsymbol{g}\cdot\boldsymbol{\tau}. \tag{3.3}$$

Following Wu (1995), the net vorticity generation rate per unit interfacial area can be determined from an interfacial vorticity balance as the sum of liquid-side and gaseous-side diffusive vorticity fluxes, given by (3.3) (assuming that the normal vector always points into the considered phase). In this balance all right-hand side terms of (3.3) except the tangential pressure derivative cancel out, due to the continuity of velocity across the interface. The vorticity generation rate is then given by the interfacial jump of the term $(1/\rho)\nabla\cdot\boldsymbol{\tau}\,p$ and thus has a baroclinic origin. Assuming, for simplicity, a constant pressure in the gaseous phase, and considering the negative tangential liquid-side pressure gradient (which follows from the positive streamwise pressure gradient and the definition of the tangential coordinate according to (3.2)) the interfacial vorticity generation rate in the CSE region must be negative, i.e. negative vorticity is produced at the interface and diffuses into both phases. In summary, the CSE region is characterized by the cross-diffusion and partial annihilation of two vorticity fluxes of opposing sign generated at the respective crosswise boundaries. Wu (1995) proposed an alternative to the concept of annihilation of vorticities of opposing sign (introduced by Morton 1984), preferring to describe the process as the dissipation of enstrophy (i.e. one half the volume integral of the square of vorticity) between the wall and the free surface.

A portion of the CSE is also seen at the top of figure 11(b). Finally, figure 11(d) shows the velocity field in the large wave, exhibiting significantly larger velocities than those in all other regions. The vector plot also shows that the crosswise velocity component is negligible in the wave crest and only increases as the flow decelerates while approaching the CSE.

After having established the velocity field topology in the different regions of the liquid film and the existence of flow separation in the capillary wave region, the following discussions concentrate on CSE dynamics. Consequently, figures 13 and 14 depict streamlines in the region of the first capillary minimum calculated from the velocity vector field measured with PIV. Thereby, figure 13 illustrates the influence of the excitation frequency on the CSE at $Re = 10.7$. As can be expected from the film thickness time traces in figures 9(d) and 9(e) the corresponding streamline patterns pictured in figures 13(a) and 13(b) do not exhibit flow separation. Indeed, for

https://doi.org/10.1017/S0022112009008155 Published online by Cambridge University Press

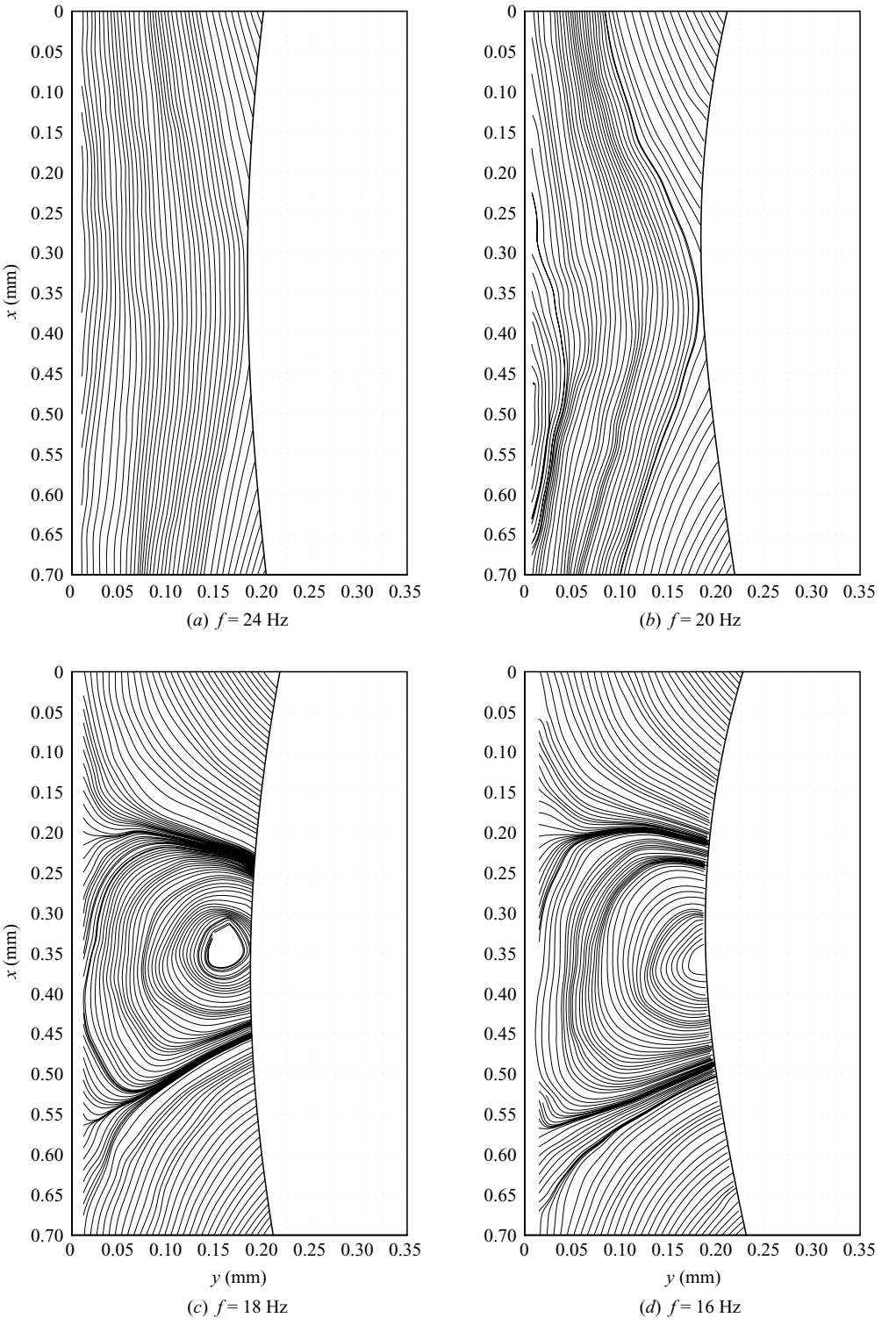
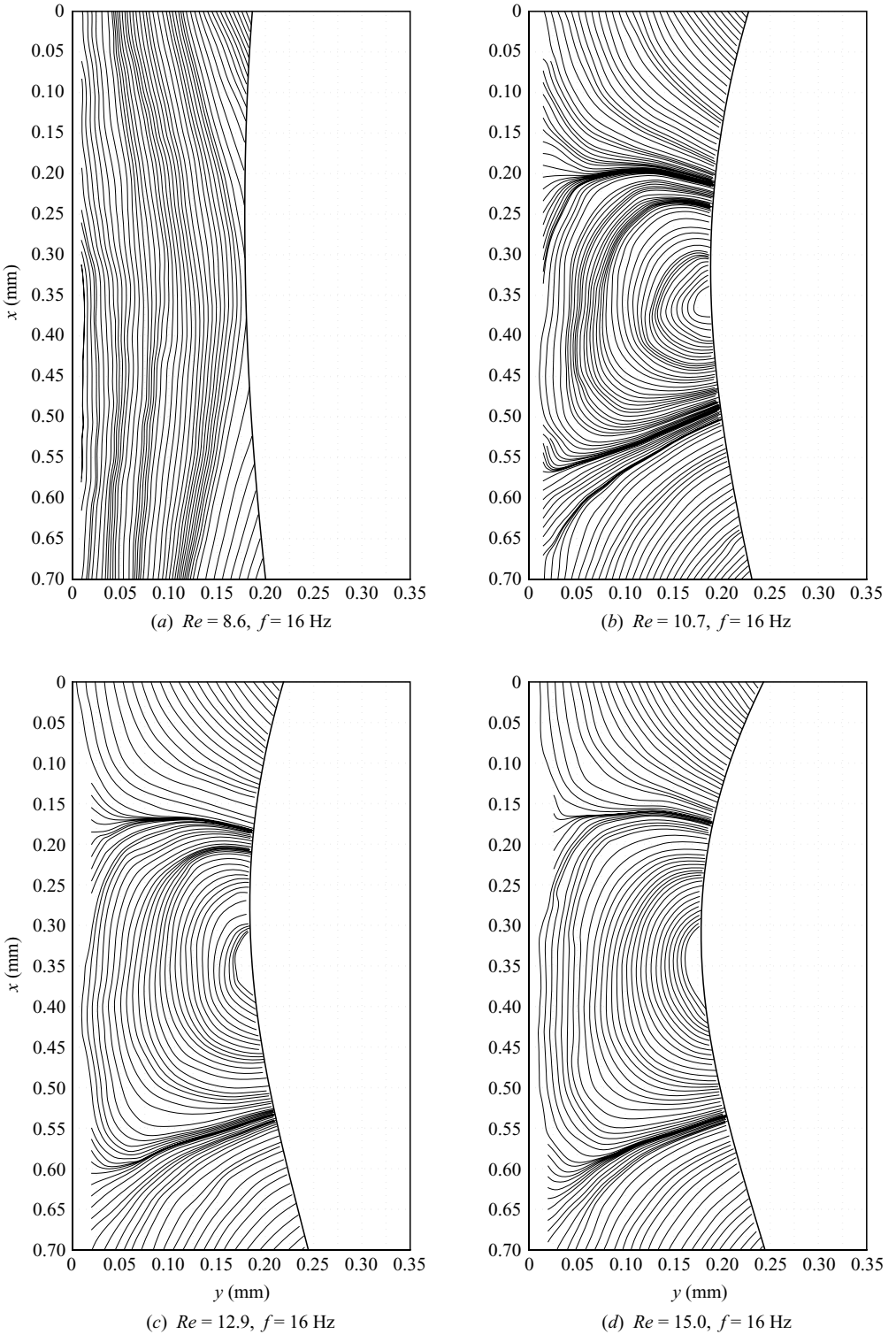


FIGURE 13. CSE dynamics: streamlines computed from PIV data and shown in the region of the first capillary minimum for different values of the excitation frequency f at $Re = 10.7$.

https://doi.org/10.1017/S0022112009008155 Published online by Cambridge University Press



(*a*) $Re = 8.6$, $f = 16$ Hz (*b*) $Re = 10.7$, $f = 16$ Hz

(*c*) $Re = 12.9$, $f = 16$ Hz (*d*) $Re = 15.0$, $f = 16$ Hz

FIGURE 14. CSE dynamics: streamlines computed from PIV data and shown in the region of the first capillary minimum for different values of the Reynolds number Re at $f = 16$ Hz (figure 14(*b*) is identical to figure 13(*d*)).

https://doi.org/10.1017/S0022112009008155 Published online by Cambridge University Press

$f = 24$ Hz the free surface of the liquid film contains no capillary waves. However, the streamline pattern in figure 13(*a*) displays flow deceleration evidenced by the streamwise progression of the streamlines which slightly leave the wall upstream of the capillary minimum and re-approach it further downstream. A similar streamline pattern can be observed in figure 13(*b*), which shows stronger flow deceleration, concurring with the existence of a single capillary wave (leading to a larger adverse pressure gradient) shown in figure 9(*d*). For $f = 18$ Hz the experimental results depicted in figure 13(*c*) show the existence of a CSE that has slightly outgrown the first capillary minimum, whereby a larger fully open CSE is encountered in figure 13(*d*). The dynamics leading from flow deceleration to CSE development and subsequent CSE–interface interaction are governed by the frequency, which acts on the separation of the large waves. Thereby, as the wave separation increases, giving way to larger stretches of residual film, capillary waves grow in number and amplitude while decreasing in wavelength (this can be roughly deduced from figures 13(*a*) to 13(*d*) and 9(*c*) to 9(*e*) and was established more clearly by Tihon *et al.* 2006). This leads to a stronger adverse pressure gradient causing a stronger deceleration of the flow. Consequently flow reversal takes place at increasing distances from the wall increasing the CSE size. Figure 14 illustrates the influence of the Reynolds number on the CSE for $f = 16$ Hz (the frequency at which capillary waves are most pronounced). As the Reynolds number increases wave separation, its effect on the CSE is contrary to that of the excitation frequency. Consequently, at the lowest Reynolds number value (see figure 14(*a*)) the flow is not separated. The streamline pattern exhibits flow deceleration similar to the conditions pictured in figures 13(*a*) and 13(*b*). Streamline patterns for all other Reynolds number values are characterized by the presence of an open CSE which increases in its streamwise dimension as the Reynolds number increases.

3.3. *Velocity field dynamics*

In addition to the velocity field measurements presented in § 3.2, time traces of the local streamwise velocity component were measured using LDV. Thereby, the Reynolds number and excitation frequency were varied in addition to the crosswise LDV measurement position which was moved from the wall to the maximal film thickness in increments of 20 μm. Further, the film thickness was measured simultaneously for all cases as close as possible to the LDV measurement position (a small streamwise offset was necessary to avoid influencing the CCI measurement with the LDV laser beams). This enables the correlation of velocity and film thickness data elucidating the effect of wave dynamics on momentum transfer in the liquid film. Figure 15 illustrates a typical set of LDV data depicting time traces of the streamwise velocity at different crosswise positions in the film for flow conditions corresponding to figure 11 (i.e. $Re = 15.0$, $f = 16$ Hz). Thereby, for figures 15(*a*)–15(*c*) the LDV measurement position lies in the residual layer of the film. The corresponding time traces display two main characteristics. First and foremost they exhibit negative values of the streamwise velocity component in each wave. This constitutes further evidence of the existence of flow reversal in falling liquid films. Thereby, the minimal velocity of the time traces corresponds to the velocities measured with PIV as can be deduced from figure 11. In fact, the deviation of PIV data (displayed in § 3.2) from LDV data for the capillary extremal values (first capillary minimum and first capillary maximum) of the streamwise velocity component is smaller than 5 % of the total change in the corresponding LDV time trace (this remaining error is of the same magnitude as the variation of LDV data between waves). Secondly, the time traces in figures 15(*a*)–15(*c*) display oscillations ahead of the main maximum which will be shown

https://doi.org/10.1017/S0022112009008155 Published online by Cambridge University Press

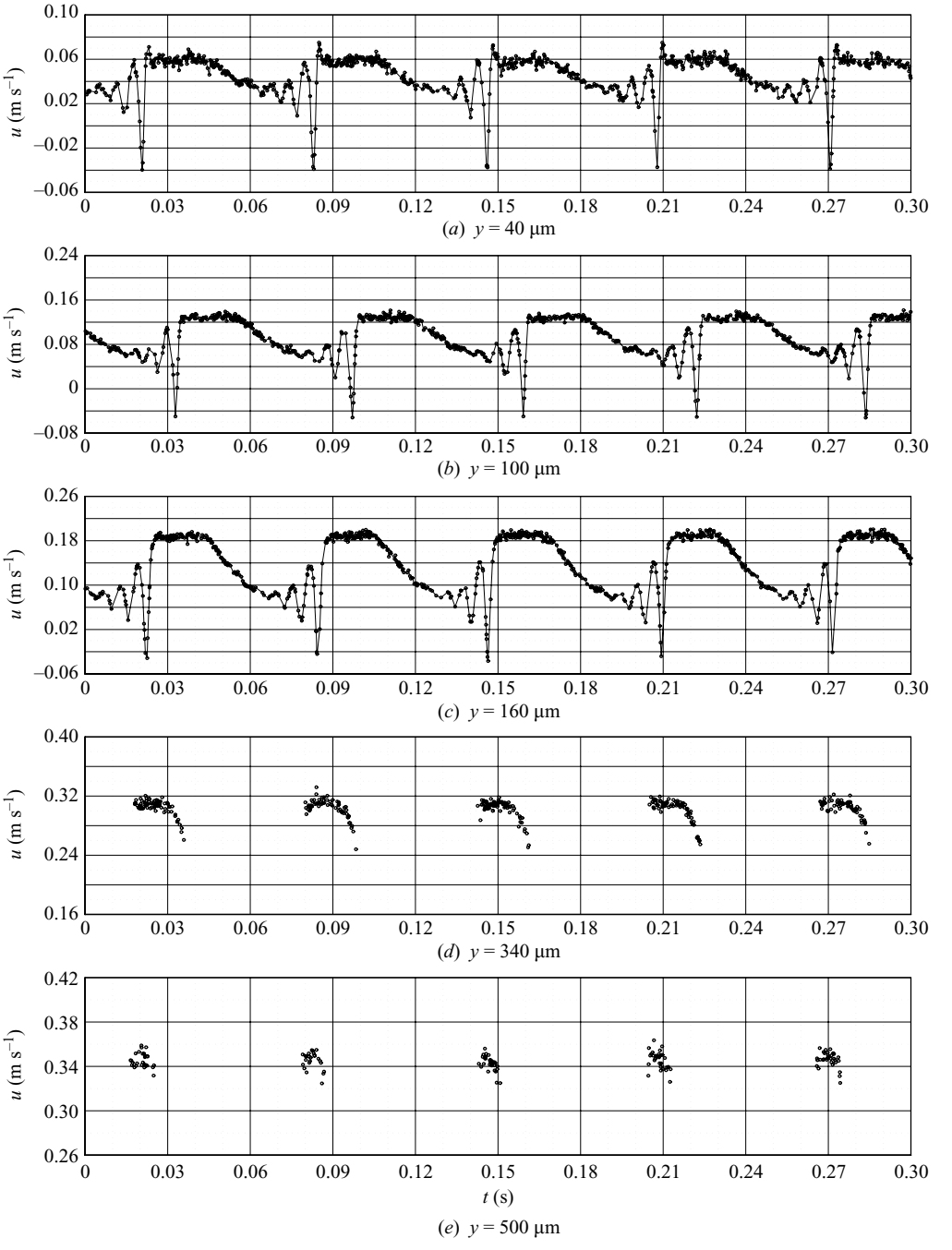


FIGURE 15. Experimental time traces of the streamwise velocity component for different crosswise positions in the liquid film: $Re = 15.0$, $f = 16$ Hz.

to correspond to the capillary waves preceding the large wave. Figures 15(d) and 15(e) depict velocity time traces at positions outside of the residual layer. These are characterized by intermittent bursts of data points as large waves pass through the LDV measurement volume separated by stretches without data when the measurement

https://doi.org/10.1017/S0022112009008155 Published online by Cambridge University Press

volume lies in the gaseous phase. In general, the LDV measurement data are shown to be reproducible as evidenced by their periodicity and to exhibit a small scatter of data points which is due to the extremely high spatial resolution of the measurement in y-direction.

In analogy to figure 13, figures 16 and 17 illustrate the excitation frequency influence on velocity time traces in the liquid film residual layer for $Re = 10.7$. The crosswise measurement position for all subfigures is $y = 0.08$ mm. At the highest excitation frequency $f = 24$ Hz (see figure 13) the time traces clearly show flow deceleration in the wave trough without exhibiting negative velocity values, which corresponds to the observations of figure 13(a). Thereby, time traces of film thickness and velocity display one maximum and one minimum in each wave. At $f = 20$ Hz, as evidenced by figure 16(b), the free surface develops a single capillary wave preceding the large wave. The corresponding velocity time trace exhibits a similar subsidiary maximum associated in time with the capillary wave. This is in accordance with the findings of figure 11 which shows that the flow is decelerated at the second capillary minimum and reaccelerated towards the first capillary maximum. Also, figure 16(b) does not display negative velocity values, concurring with the absence of flow separation in the streamline pattern of figure 13(b). Figure 17(a) ($f = 18$ Hz) shows the appearance of a second capillary wave which leads to a second subsidiary minimum in the velocity time trace. Further, the velocity time trace exhibits slightly negative velocity values. Time traces depicted in figure 17(b) for $f = 16$ Hz show the same principle behaviour as those in figure 17(a) with the exception that a third capillary wave and associated subsidiary velocity maximum appear. In addition, the velocity time trace attains larger negative values. The presence of negative velocity data in figures 17(a) and 17(b) concurs with the existence of capillary flow separation in the corresponding streamline patterns (see figures 13(c) and 13(d)).

Figures 18 and 19 illustrate the Reynolds number influence on velocity time traces in the liquid film residual layer ($y = 0.12$ mm) for $f = 16$ Hz. Thereby, different subfigures correspond to the streamline patterns of figure 14. For all Reynolds number values except $Re = 8.6$ the velocity time traces exhibit a sign change at the first capillary minimum concurring with the CSE shown in figures 14(b)–14(d). For $Re = 8.6$, though the flow is strongly decelerated, the streamwise velocity is permanently positive which is in accordance with figure 14(a). It is discernible from figures 18 and 19 that an increase in the Reynolds number increases the number of subsidiary velocity maxima while reducing the global minimum and increasing the global maximum of the velocity time trace.

In summary, figures 16–19 show that velocity time traces in the residual layer are closely correlated with the temporal evolution of film thickness. This is for example evidenced by the fact that the number of subsidiary velocity time trace minima is equivalent to the number of capillary waves. It is thus the free surface topology through its capillary effect on the pressure distribution that governs the velocity field in the residual layer and more importantly in the capillary wave region. This is not surprising as in this region capillary forces dominate viscous forces. Moreover the LDV results show in a reproducible manner that flow reversal takes place in the capillary wave region.

4. Numerical results

As stated before, experiments were performed in the developed region of the falling liquid film, yielding no information regarding the spatio-temporal evolution

https://doi.org/10.1017/S0022112009008155 Published online by Cambridge University Press

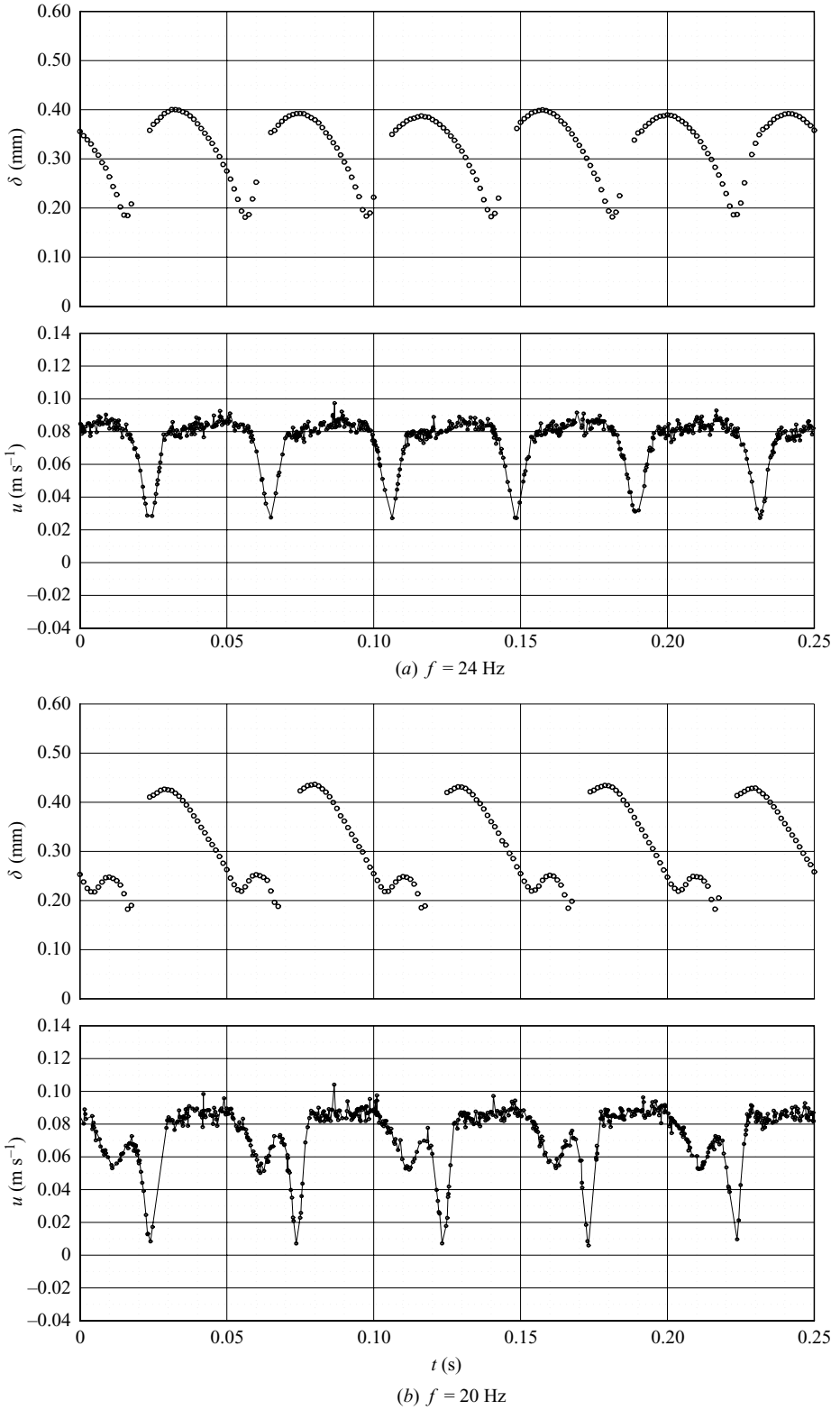
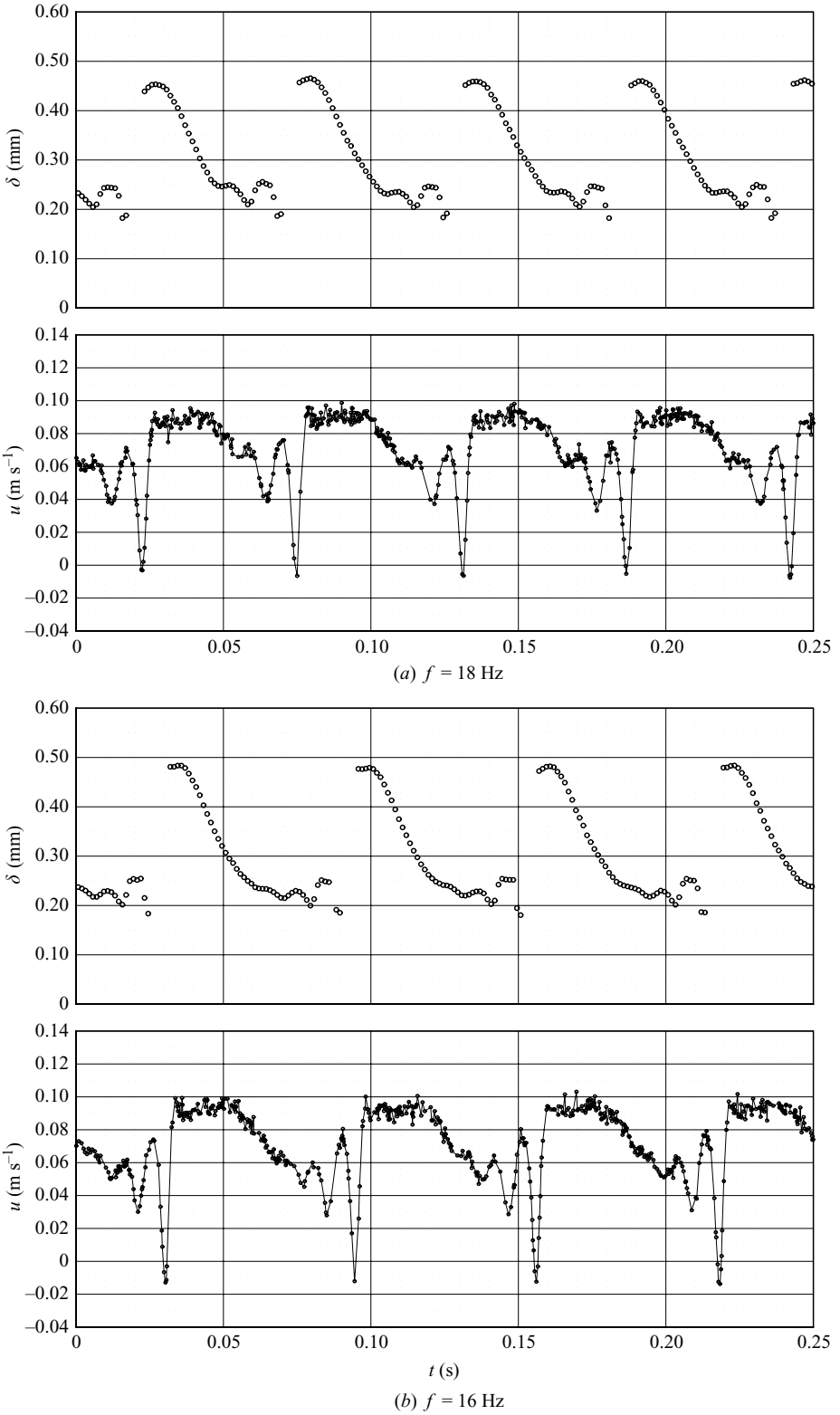


FIGURE 16. Experimental time traces of film thickness and streamwise velocity component for different excitation frequencies ($f = 20, 24$ Hz): $Re = 10.7$, $y = 0.08$ mm.

https://doi.org/10.1017/S0022112009008155 Published online by Cambridge University Press

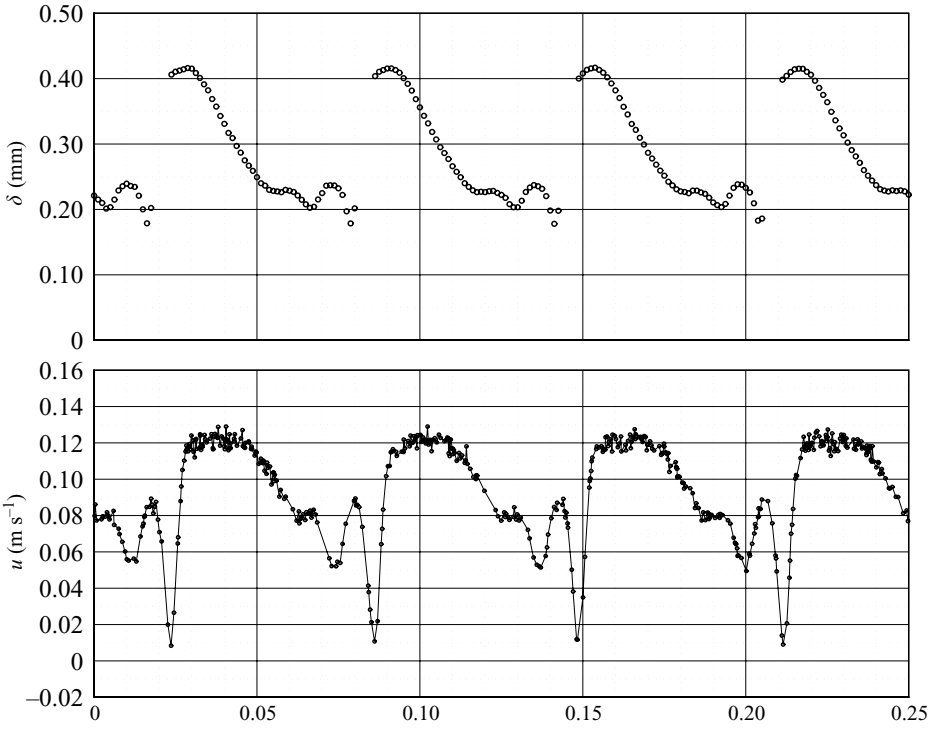


(*a*) $f = 18$ Hz

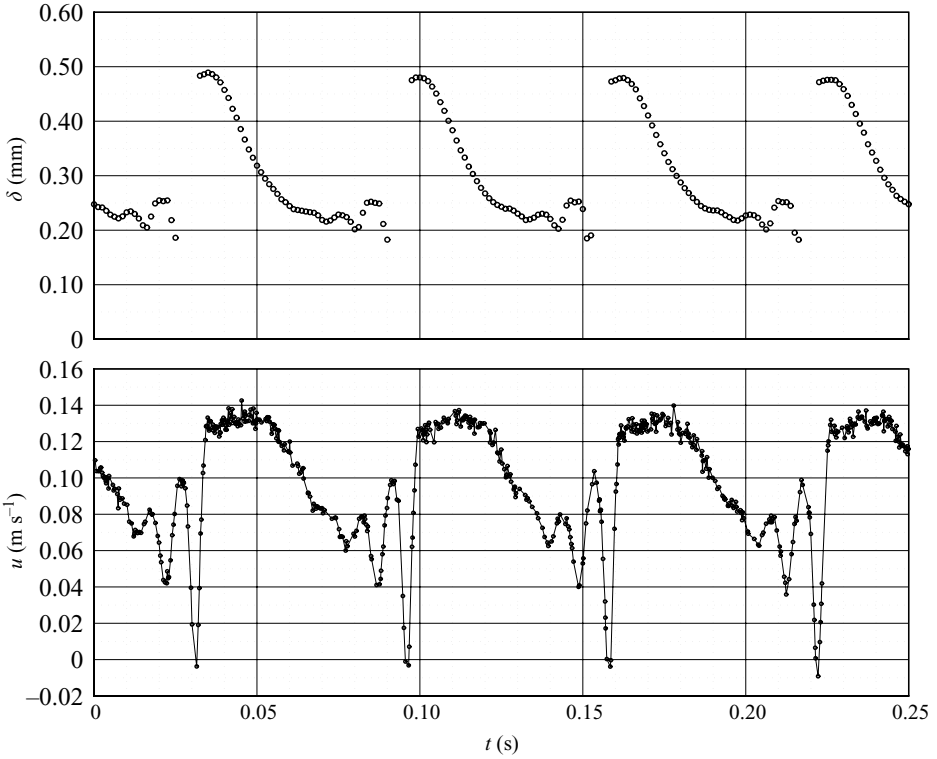
(*b*) $f = 16$ Hz

FIGURE 17. Experimental time traces of film thickness and streamwise velocity component for different excitation frequencies ($f = 16, 18$ Hz): $Re = 10.7$, $y = 0.08$ mm.

https://doi.org/10.1017/S0022112009008155 Published online by Cambridge University Press



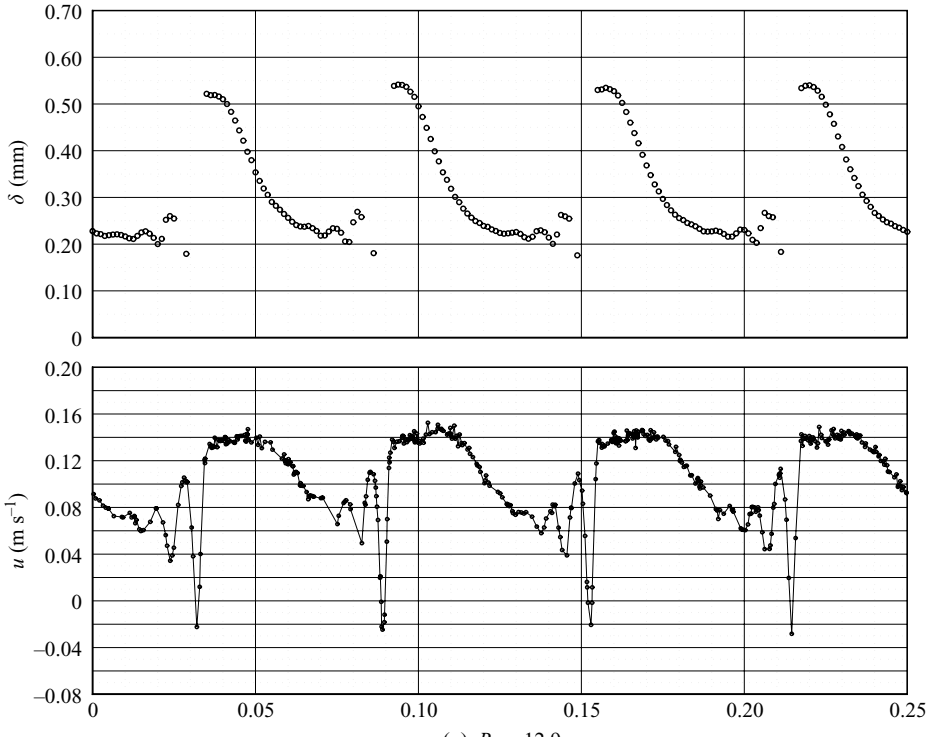
(*a*) $Re = 8.6$



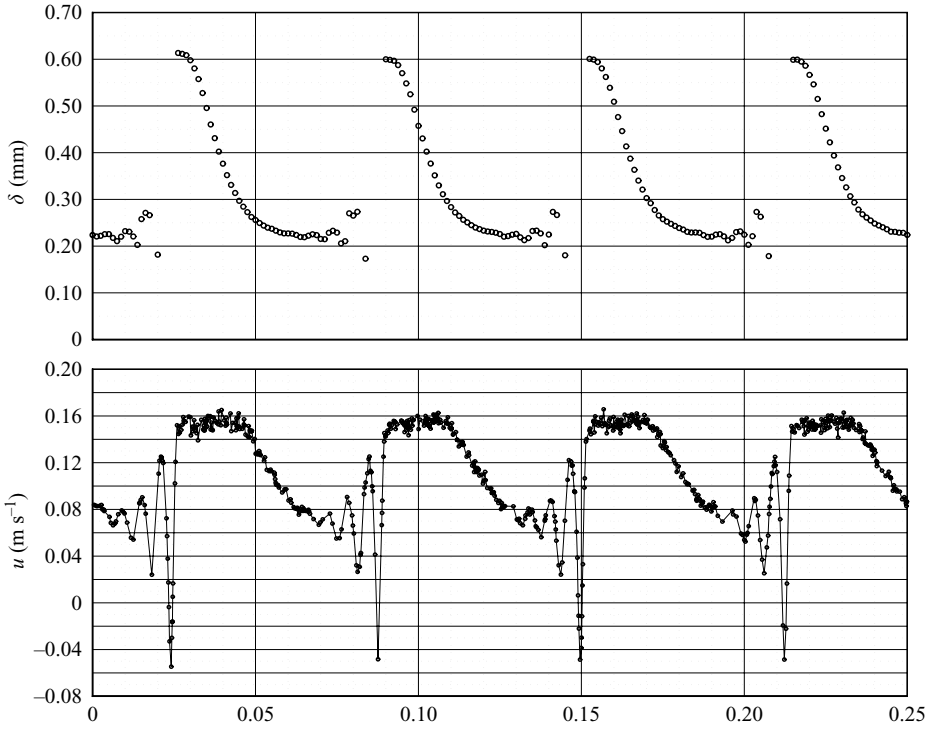
(*b*) $Re = 10.7$

FIGURE 18. Experimental time traces of film thickness and streamwise velocity component for different Reynolds number values ($Re = 8.6, 10.7$): $f = 16$ Hz, $y = 0.12$ mm.

https://doi.org/10.1017/S0022112009008155 Published online by Cambridge University Press



(*a*) $Re = 12.9$



(*b*) $Re = 15.0$

FIGURE 19. Experimental time traces of film thickness and streamwise velocity component for different Reynolds number values ($Re = 12.9, 15.0$): $f = 16$ Hz, $y = 0.12$ mm.

https://doi.org/10.1017/S0022112009008155 Published online by Cambridge University Press

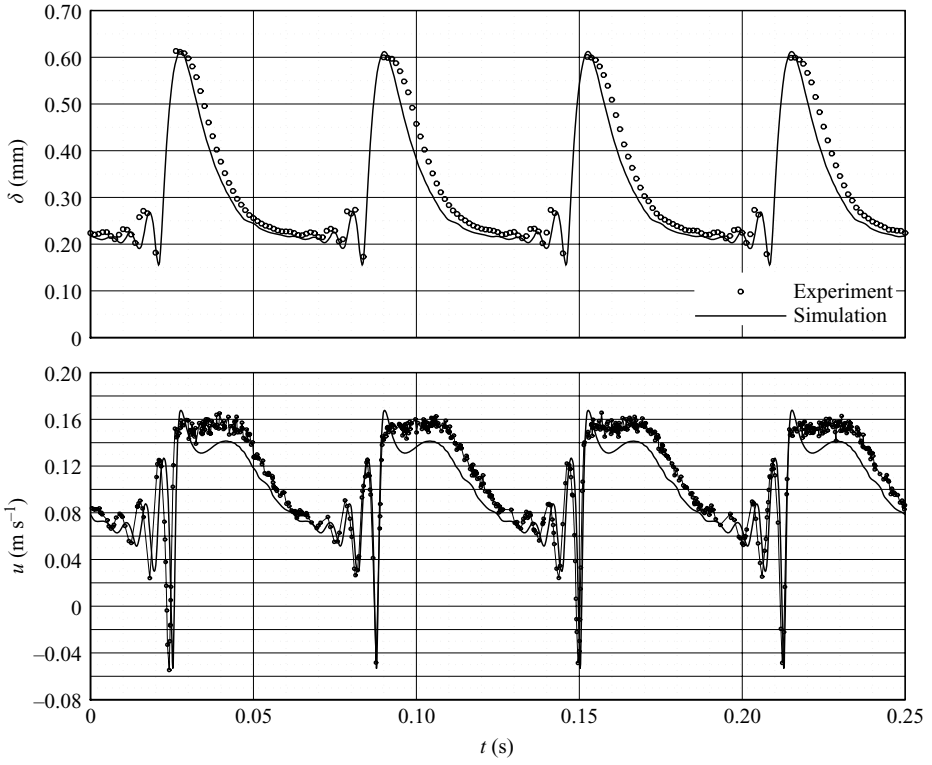


FIGURE 20. Comparison of numerical and experimental data: time traces of film thickness and streamwise velocity component for $Re = 15$, $f = 16$ Hz and $y = 0.12$ mm.

of the CSE. In order to complement experimental data, numerical simulation results of the falling liquid film are presented here. Thereby, the same numerical methods as described in Dietze *et al.* (2008) were employed (the formulation of the outlet boundary condition was modified to allow for liquid backflow into the calculation domain). The two-dimensional simulation was performed for $Re = 15$ and $f = 16$ Hz using fluid properties of the DMSO–water solution listed in table 1. The spatial resolution in streamwise and crosswise direction is $\Delta_x = 0.05$ mm and $\Delta_y = 0.02$ mm and the temporal resolution $\Delta_t = 5 \times 10^{-6}$ s. Figure 20 compares experimental and numerical film thickness and streamwise velocity time traces in the developed region of the film. Agreement between the data sets is good in general and particularly so in the capillary wave region where the CSE phenomenon arises. Figure 21 shows a series of streamline patterns in the region of the first capillary minimum at different times in the surface wave development. The first four pictures show the deceleration and subsequent separation of the flow yielding a closed CSE growing in size as the capillary wave develops. When the size of the CSE attains the minimal film thickness it is broken up into an open shape as shown in figure 21(*a*). This transition itself influences the capillary wave topology causing the CSE to contract into a closed shape once again (see figure 21(*f*)). Figures 21(*g*) and 21(*h*) show the CSE as it is subsequently forced into its developed open shape by the primary wave dynamics. Thereby, figure 21(*h*) yields good agreement with the corresponding experimental streamline pattern in figure 14(*d*).

https://doi.org/10.1017/S0022112009008155 Published online by Cambridge University Press

https://doi.org/10.1017/S0022112009008155 Published online by Cambridge University Press

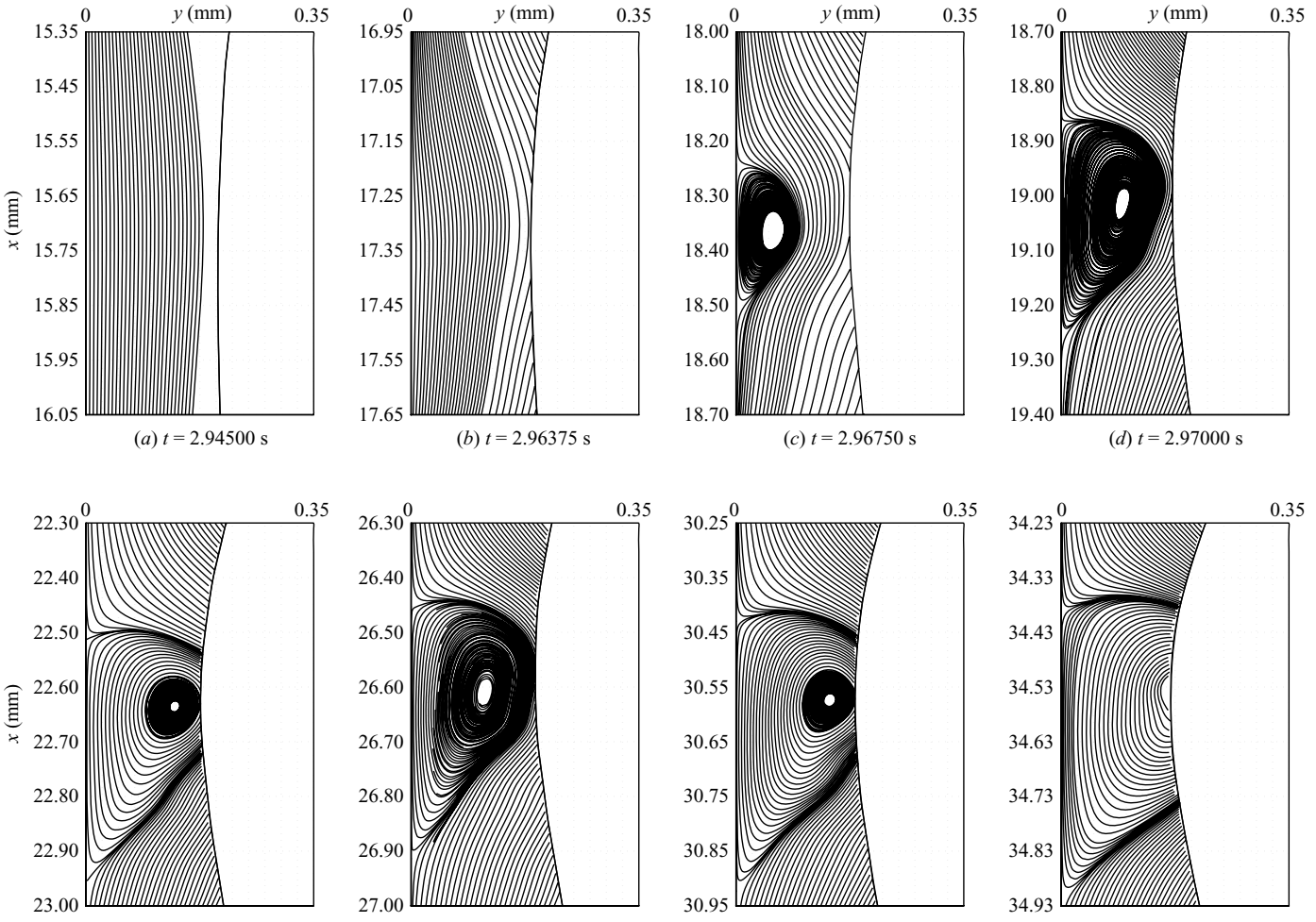


FIGURE 21. Streamlines in the capillary wave region computed from numerical data: $Re = 15$, $f = 16$ Hz.

5. Conclusion

Spatially and temporally highly resolved velocity and film thickness measurements in two-dimensional falling liquid films with externally excited surface waves were performed in a specifically designed optical test section. Characteristically, the refractive index of the working fluid and that of the glass body on which the falling film develops were matched, allowing optimal access for the employed optical measurement techniques. The set-up allows for an unprecedented spatial and temporal resolutions of the dynamics of the velocity field in the liquid film. Thereby, PIV was used to measure the velocity field in the cross-section of the film with a repetition rate of up to 4500 Hz and LDV was employed to measure time traces of the streamwise velocity component yielding a spatial resolution of 25 μm and a data rate of up to 3000 Hz. The film thickness was measured with a CCI technique. Attention has been directed to obtaining clear experimental proof of flow separation in the capillary wave region published in a previous work by Dietze *et al.* (2008). Therefore experiments were performed for a range of Reynolds number and frequency values with an aqueous dimethylsulfoxide solution. PIV results clearly show the existence of a CSE as shown in the stated publication for specific flow regimes. The dynamics of the CSE were found to depend on the characteristics of the capillary waves which themselves are governed by the separation of the large wave humps they precede. This wave separation increases with increasing Reynolds number and decreasing excitation frequency thereby increasing the number of capillary waves as well as their amplitude while decreasing their wavelength. As a result, according to Dietze *et al.* (2008) the adverse pressure gradient at the first capillary minimum (where the change in curvature of the free surface is the strongest) increases. Consequently, the flow in this region was found to transit three stages with increasing wave separation starting with mere flow deceleration followed by flow separation yielding the CSE which is first contained in the liquid film and in the third stage develops into an open vortex with streamlines ending at the free surface. Further, the velocity field in different regions of the falling film was elucidated, showing that flow deceleration and reacceleration takes place in all capillary waves giving streamlines a wavy shape similar to that of the free surface. LDV time traces in the residual layer confirm the existence of flow reversal at the first capillary minimum. Further, it was shown that velocity time traces in the residual layer are closely correlated with film thickness time traces. Thereby, a subsidiary velocity maximum is associated with each capillary wave owing to the adverse pressure gradient developing in each capillary minimum. The large wave hump leads to an equally large maximum in the velocity time trace. The effect of increasing wave separation (caused by increasing Reynolds number or decreasing excitation frequency) on the velocity time traces is characterized by stronger deceleration and reacceleration of the flow in the different capillary waves as well as the appearance and intensification of flow reversal in the first capillary minimum. The work constitutes a logical continuation of a previous publication by Dietze *et al.* (2008) confirming its main findings on the CSE phenomenon experimentally. The results are of potential interest in the context of developing simplified models for momentum and wave dynamics of falling liquid films, specifically with respect to the formulation of physically sound approximations of the crosswise profile of the streamwise velocity component. For the future, simultaneous measurements of the streamwise and crosswise velocity components in the liquid film using a two-colour LDV system are envisaged. Such measurements are possible in the optical test section presented in this paper. Further, attention will be directed to

https://doi.org/10.1017/S0022112009008155 Published online by Cambridge University Press

the investigation of the velocity field in the residual layer for more technically relevant flow regimes characterized by three-dimensional wave dynamics and turbulence.

The authors gratefully acknowledge the financial support of the Deutsche Forschungsgemeinschaft (DFG) within the Collaborative Research Center (SFB) 540 'Model-based Experimental Analysis of Kinetic Phenomena in Fluid Multi-phase Reactive Systems'.

REFERENCES

Adomeit, P., Leefken, A. & Renz, U. 2000 Experimental and numerical investigations on wavy films. In *Proceedings of the 3rd European Thermal Sciences Conference* (ed. E. W. P. Hahne, W. K. Heidemann & K. Spindler), vol. 2, pp. 1003–1009. Heidelberg. ETS.

Adomeit, P. & Renz, U. 2000 Hydrodynamics of three-dimensional waves in laminar falling films. *Intl J. Multiphase Flow* **26**, 1183–1208.

Albrecht, H. E., Borys, M., Damaschke, N. & Tropea, C. 2003 *Laser Doppler and Phase Doppler Measurement Techniques*. Springer.

Alekseenko, S. V., Antipin, V. A., Bobylev, A. V. & Markovich, D. M. 2007 Application of PIV to velocity measurements in a liquid film flowing down an inclined cylinder. *Exp. Fluids* **43** (2–3), 197–207.

Alekseenko, S. V., Nakoryakov, V. E. & Pokusaev, B. G. 1994 *Wave Flow of Liquid Films*. Begell House Inc.

Budwig, R. 1994 Refractive index matching methods for liquid flow investigations. *Exp. Fluids* **17**, 350–355.

Chang, H. C. & Demekhin, E. A. 2002 *Complex Wave Dynamics on thin Films*. Studies in Interface Science, vol. 14. Elsevier.

Cohen-Sabban, J., Gaillard-Groleas, J. & Crepin, P.-J. 2001 Quasi-confocal extended field surface sensing. In *Proceedings of SPIE* (ed. A. Duparre & B. Singh), Optical Metrology Roadmap for the Semiconductor, Optical, and Data Storage Industries II, vol. 4449, pp. 178–183. SPIE.

Dietze, G. F., Leefken, A. & Kneer, R. 2008 Investigation of the back flow phenomenon in falling liquid films. *J. Fluid Mech.* **595**, 435–459.

Elsässer, A. 1998 Kraftstoffaufbereitung in Verbrennungskraftmaschinen: Grundlagen der Strömung schubspannungsgetriebener Wandfilme. PhD thesis, Technische Universität Karlsruhe.

Gao, D., Morley, N. B. & Dhir, V. 2003 Numerical simulation of wavy falling film flow using VOF method. *J. Comput. Phys.* **192**, 624–642.

Green, S. I. 1996 *Fluid Vortices*, chapter 1, p. 22. Kluwer Academic Publishers.

Hjelmfelt, A. T. & Mockros, L. F. 1966 Motion of discrete particles in a turbulent fluid. *Appl. Sci. Res.* **16**, 149–161.

Kapitza, P. L. 1948 Wave flow of thin layers of a viscous fluid (in Russian). *Zhurn. Eksper. Teor. Fiz.* **3** (1), 3–28.

Kunugi, T. & Kino, C. 2005 DNS of falling film structure and heat transfer via MARS method. *Comp. Struct.* **83** (6–7), 455–462.

Kunugi, T., Kino, C. & Serizawa, A. 2005 Surface wave structure and heat transfer of vertical liquid film flow with artificial oscillation. In *5th International Symposium on Multiphase Flow, Heat Mass Transfer and Energy Conversion*. Article no. 71. Xi'an, China.

Leefken, A., Al-Sibai, F. & Renz, U. 2004 LDV measurement of the velocity distribution in periodic waves of laminar falling films. In *Proceedings of the 5th International Conference on Multiphase Flow*. Article no. 520. Yokohama, Japan.

Lel, V. V., Al-Sibai, F. & Leefken, A. 2005 Local thickness and wave velocity measurement of wavy films with a chromatic confocal imaging method and a fluorescence intensity technique. *Exp. Fluids* **39** (5), 856–864.

https://doi.org/10.1017/S0022112009008155 Published online by Cambridge University Press

Liu, J., Paul, J. D. & Gollub, J. P. 1993 Measurements of the primary instabilities of film flows. *J. Fluid Mech.* **250**, 69–101.

Luff, J. D., Drouillard, T., Rompage, A. M., Linne, M. A. & Hertzberg, J. R. 1999 Experimental uncertainties associated with particle image velocimetry (PIV) based vorticity algorithms. *Exp. Fluids* **26**, 36–54.

Lundgren, T. & Koumoutsakos, P. 1999 On the generation of vorticity at a free surface. *J. Fluid Mech.* **382**, 351–366.

Malamataris, N. A. & Balakotaiah, V. 2008 Flow structure underneath the large amplitude waves of a vertically falling film. *AIChE J.* **54** (7), 1725–1740.

Miyara, A. 1999 Numerical analysis on flow dynamics and heat transfer of falling liquid films with interfacial waves. *Heat Mass Transfer* **35**, 298–306.

Morton, B. R. 1984 The generation and decay of vorticity. *Geophys. Astrophys. Fluid Dyn.* **28**, 277–308.

Mudawar, I. & Houpt, R. A. 1993*a* Mass and momentum transport in smooth falling liquid films laminarized at relatively high Reynolds numbers. *Intl J. Heat Mass Transfer* **36** (14), 3437–3448.

Mudawar, I. & Houpt, R. A. 1993*b* Measurement of mass and momentum transport in wavy-laminar falling liquid films. *Intl J. Heat Mass Transfer* **36** (17), 4151–4162.

Mudunuri, R. R. & Balakotaiah, V. 2006 Solitary waves on thin falling films in the very low forcing frequency limit. *AIChE J.* **52** (12), 3995–4003.

Nosoko, P., Yoshimura, P. N., Nagata, T. & Oyakawa, K. 1996 Characteristics of two-dimensional waves on a falling liquid film. *Chem. Engng Sci.* **51** (5), 725–732.

Nusselt, W. 1916 Die Oberflächenkondensation des Wasserdampfes. *VDI-Zeitschrift* **60**, 541–546.

Portalski, S. 1964 Eddy formation in film flow down a vertical plate. *Ind. Engng Chem. Fundam.* **3** (1), 49–53.

Raffel, M., Willert, C., Wereley, S. & Kompenhans, J. 2007 *Particle Image Velocimetry: A Practical Guide*, 2nd edn. Springer-Verlag.

Rood, E. P. 1994 Interpreting vortex interactions with a free surface. *J. Fluids Engng* **116**, 91–94.

Scheid, B., Ruyer-Quil, C. & Manneville, P. 2006 Wave patterns in film flows: modelling and three-dimensional waves. *J. Fluid Mech.* **562**, 183–222.

Tihon, J., Serifi, K., Argyriadi, K. & Bontozoglou, V. 2006 Solitary waves on inclined films: their characteristics and the effects on wall shear stress. *Exp. Fluids* **41**, 79–89.

Trevelyan, P. M. J., Scheid, B., Ruyer-Quil, C. & Kalliadasis, S. 2007 Heated falling films. *J. Fluid Mech.* **592**, 295–334.

Westerweel, J. 1994 Efficient detection of spurious vectors in particle image velocimetry data. *Exp. Fluids* **16**, 236–247.

Wu, J.-Z. 1995 A theory of three-dimensional interfacial vorticity dynamics. *Phys. Fluids* **7** (10), 2375–2395.

https://doi.org/10.1017/S0022112009008155 Published online by Cambridge University Press